



CHALMERS
UNIVERSITY OF TECHNOLOGY

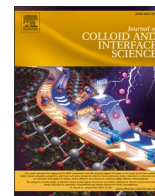
Thermally stable electrolyte for lithium-oxygen battery and its metal-free version

Downloaded from: <https://research.chalmers.se>, 2025-12-24 13:21 UTC

Citation for the original published paper (version of record):

Levchenko, S., Barcaro, E., Comini, A. et al (2026). Thermally stable electrolyte for lithium-oxygen battery and its metal-free version. *Journal of Colloid and Interface Science*, 706.
<http://dx.doi.org/10.1016/j.jcis.2025.139622>

N.B. When citing this work, cite the original published paper.



Thermally stable electrolyte for lithium-oxygen battery and its metal-free version

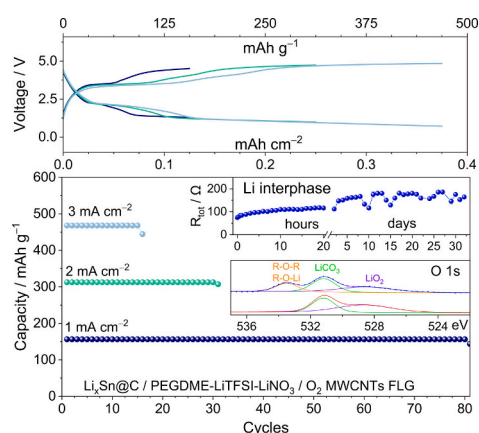
Stanislav Levchenko^{a,1}, Edoardo Barcaro^{a,1}, Alessio Comini^a, Aleksandar Matic^b, Jusef Hassoun^{a,c,*}

^a Department of Chemical, Pharmaceutical and Agricultural Sciences, University of Ferrara, Via Fossato di Mortara 17, Ferrara 44121, Italy

^b Department of Physics, Chalmers University of Technology, SE 412 96, Gothenburg, Sweden

^c Graphene Labs, Istituto Italiano di Tecnologia, via Morego 30, Genoa 16163, Italy

GRAPHICAL ABSTRACT



ARTICLE INFO

Keywords:

Li-O₂
Li-ion
PEGDME
LiNO₃
High-energy

ABSTRACT

Polyethylene glycol dimethyl ether with molecular weight of 250 (PEGDME 250) is considered a solvent of choice to achieve electrolytes with low volatility and high thermal stability for application in lithium oxygen (Li-O₂) cells. The study focuses on the concomitant effect of the conducting salt lithium bis(trifluoromethanesulfonyl)imide (LiTFSI) and the sacrificial film-forming salt lithium nitrate (LiNO₃) both on chemical and electrochemical features. The electrolytes reveal conductivity ranging from $\sim 10^{-3}$ S cm⁻¹ at 85 °C to $\sim 10^{-4}$ S cm⁻¹ at -7 °C, and Li⁺ transference number (t_+) approaching 0.6. The concomitant incorporation of LiTFSI and LiNO₃ significantly modifies the thermal characteristics of the electrolyte due to specific salt-solvent interactions. Furthermore, LiNO₃ actually enhances the solid electrolyte interphase (SEI), stabilizes the Li, and improves the conductivity below 61 °C without significantly altering the t_+ value. Despite the Li-O₂ cell can operate suitably even without LiNO₃ addition where a capacity limit of 0.5 mAh cm⁻² (500 mAh g⁻¹) is exploited, the one added by LiNO₃ can reversibly deliver a higher capacity (4500 mAh g⁻¹, 5.4 mAh cm⁻²) than

* Corresponding author.

E-mail address: jusef.hassoun@unife.it (J. Hassoun).

¹ Authors equally contributed.

<https://doi.org/10.1016/j.jcis.2025.139622>

Received 15 March 2025; Received in revised form 29 November 2025; Accepted 2 December 2025

Available online 3 December 2025

0021-9797/© 2025 The Authors. Published by Elsevier Inc. This is an open access article under the CC BY license (<http://creativecommons.org/licenses/by/4.0/>).

the bare solution (2000 mAh g⁻¹, 2.2 mAh cm⁻²) if the voltage cutoff is used. On the other hand, the solution added by LiNO₃ enhances the performance of the metal-free (Li-ion) version of the cell using O₂ and Li₃Sn@C alloying anode, with capacity ranging from 50 to 450 mAh g⁻¹ delivered at currents from 0.1 to 3 mA cm⁻². These findings may favor the achievement of high-energy storage systems with low cost and environmental sustainability.

1. Introduction

1.1. The battery demand for energy storage

European Green Deal was launched in 2019 by the EU commission, to achieve net-zero CO₂ emissions until 2050, and reach for first the climate-neutral condition. Key strategies to match this ambitious target involved reforming the energy policies and adapting the internal market to accommodate renewable sources [1]. Additionally, in June 2022 the EU decided a crucial restriction of the internal combustion engines by 2035 [2]. Therefore, the demand for batteries to power electric vehicles (EVs) has been predicted to increase by 5 times on 2030 and by 15 times on 2050, to substantially support the transition to a more sustainable transportation [3]. In this view, a recent work indicated that the battery demand in Europe can exceed 1.0T Wh per year by 2030, thus outpacing the domestic production and requiring growth rates from 31 % to 68 % per year. Hence, the research suggested production capability acceleration by the stakeholders to match the demand growth post-2030, with reliable industrial policies [4]. Meanwhile, the need for EVs with extended driving range triggered the request for efficient energy storage systems such as the lithium-ion (Li-ion) battery, which is currently the most widely diffused power source. These batteries rely on critical metals such as nickel, manganese, and cobalt, which pose significant environmental and economic concerns, in particular considering their limited and geographically localized availability, and the rising price due to growing demand [5,6]. This scenario not only suggested the crucial importance of the re-use of spent batteries, degradation diagnostics, and materials recovery, but also the need for more suitable energy storage systems [7]. Among the various systems, metal-air batteries in which the oxygen electrochemically reacts with a metal having a low redox potential such as Zn, Al, Na or Li appeared the most promising candidates in terms of low cost, sustainability and high energy density [8–10].

1.2. The Li–O₂ battery

Non-aqueous Li–O₂ battery represented one of the most energetic and intriguing systems for several demanding fields, including the EVs market [11,12]. This battery operates according to the overall reaction $2\text{Li} + \text{O}_2 \rightleftharpoons \text{Li}_2\text{O}_2$, which is a multi-step process evolving at 2.9 V with the impressive theoretical energy density of 3400 Wh kg⁻¹ and 8050 Wh L⁻¹ [11,12]. Typically, the O₂ gas is hosted *ad hoc* into a gas diffusion layer (GDL) coated with carbon-based materials, such as nanotubes, graphene, or hard carbons, and often combined with various catalysts optimized to enhance the formation of Li₂O₂ by oxygen reduction reaction (ORR) and its dissolution by oxygen evolution reaction (OER) during cycling [13–16]. Another crucial component of the Li–O₂ battery is the electrolyte which should be lowly volatile, as well as thermally and chemically stable. Recent improvements of glyme, polymer, and ionic liquid electrolytes have played key role in facilitating and triggering the research and development of Li–O₂ battery [17–20]. Indeed, the traditional electrolytes employed in Li-ion battery, typically based on organic carbonate solvents, can easily undergo parasitic reaction and degradation against the highly reactive and nucleophile intermediates formed during Li–O₂ cell operation, such as superoxide radicals and the peroxide itself [20]. Glyme solvents have been suggested to be particularly advantageous in Li–O₂ batteries as they can stabilize the superoxide ion by forming complexes such as

[Li⁺(solvent)_n⋯O₂⁻], thus enhancing the reversibility of the cell and mitigating the side reactions [21]. A significant limitation of the Li–O₂ cell may be represented by the use of lithium metal as the anode with possible formation of non-uniform SEI during charge and discharge cycles. This uneven SEI growth can facilitate the development of dendritic structures penetrating the separator until possible internal short circuits within the cell, with serious safety risks hindering the practical battery application [22]. The addition of sacrificial agents, such as vinylene carbonate (VC), LiNO₃, or (MgNO₃)₂, in the electrolyte has been indicated as a potential strategy to form more stable and uniform SEI, limit dendrite growth, reduce lithium reactivity, and finally enhance the overall safety and cycle life of the cell [23–25]. Another effective approach has suggested the use of hollow nanospheres or porous current collectors to better tune the electric field, thereby limiting the local current density on the lithium surface [26–28]. Furthermore, the deposition of materials such as hexagonal boron nitride (h-BN) or silicon oxide at the lithium surface can create a physical barrier to limit the growth and spread of dendrites [29,30]. The most alternative pathway to avoid the challenges associated with Li has foreseen the complete replacement of the alkali metal anode with conversion or alloying anodes, based on Fe, Cu, Sn, Sb, or Si, to achieve the Li-ion configuration using the oxygen cathode, offering enhanced safety and stability by almost suppressing the above mentioned risks [11,31].

1.3. Aim of the work

In this work, we investigated the performance of electrolytes based on PEGDME 250 with LiTFSI and LiNO₃ salts in Li–O₂ cells. The PEGDME 250 is selected due to its enhanced safety profile, including lower flammability, higher flash point, and reduced toxicity compared to glymes with lower molecular weight such as TREGDME and TEGDME, which have already shown excellent cyclability and film formation ability in Li–O₂ battery [14,32,33]. These characteristics suggested PEGDME 250 as a very promising candidate for use as a green and sustainable electrolyte solvent [34]. Initially, the electrolytes have been analyzed using various techniques to examine their physical-chemical properties. Subsequently, a range of electrochemical measurements has been employed to investigate their conductivity, stability window, and lithium-ion transference number. Then the electrolytes have been tested in Li–O₂ cells, combining multiwalled carbon nanotubes (MWCNTs) and few-layer graphene (FLG) as the cathodic material. This cathode setup has been previously studied in combination with TEGDME-based electrolytes, providing a benchmark for comparison [15]. Finally, Li-ion-O₂ cells have been achieved with a lithiated Sn@C anode, which was investigated for application in Li-ion cells elsewhere [35], and studied under various currents and operating regimes to demonstrate their actual applicability upon a careful control and possible protection of the anode/electrolyte interphase. Electrochemical tests combined with *ex-situ* measurements on the electrodes have been also carried out to demonstrate the occurrence of the reversible OER/OER reaction and the interphase characteristics.

2. Experimental section

2.1. Electrolyte preparation

Two electrolyte solutions were prepared by dissolving either LiTFSI alone, or LiTFSI and LiNO₃ (both 99.99 % trace metals basis, Sigma-

Aldrich) in PEGDME 250 (average M_n 250, Sigma-Aldrich) at a concentration of 1 mol of each salt in a 1 kg of solvent. The first electrolyte was referred in the text as PEGDME 250 LiTFSI 1 m, while the second one as PEGDME 250 LiTFSI 1 m LiNO₃ 1 m. Before preparing the electrolytes, LiTFSI and LiNO₃ salts were dried under vacuum at 110 °C for 2 days. The PEGDME 250 solvent was stored in an Ar-filled glovebox with *extra-dry* molecular sieves (0.3 nm, rods, ~1.6 mm diameter, Sigma-Aldrich) for at least one week. The *extra-dry* condition of the sieves was previously achieved by heating them under vacuum at 240 °C for 5 days. Before preparing the electrolyte, the water content of the PEGDME 250 was verified by an 899 Karl Fischer Coulometer (Metrohm) to be below 30 ppm.

2.2. Synthesis of MWCNTs/FLG 50:50 cathodic material and Sn@C anodic material

The cathodic material for hosting the oxygen of the Li—O₂ cells was prepared as described previously [15]. In brief, commercial MWCNTs (>90 % carbon basis, D × L: 110–170 nm × 5–9 μm, Sigma-Aldrich) and FLG produced by the wet-jet milling (BeDimensional S.p.A.) [36] were combined into a 50:50 weight ratio in tert-butanol/distilled water (6:4 weight ratio), stirred, and sonicated at 50 °C to promote liquid-phase exfoliation of FLG and separation of carbon nanotubes, dried at 65 °C, and finally annealed under nitrogen at 750 °C for activation. The Sn@C composite was prepared as reported in a previous paper [35]. Nanometric Sn and sucrose were combined in water, heated at 50 °C under magnetic stirring until full evaporation, annealed in a tube furnace at 700 °C for 3 h under an Ar/H₂ (5 % H₂) atmosphere, and then cooled to room temperature and grinded. The Sn to C weight ratio into the final composite was of approximately 1:2.

2.3. Electrode preparation

Electrodes for voltammetry tests were prepared by dispersing SP Carbon (SPC, Timcal) and Polyvinylidene Fluoride (PVDF 6020, Solvay) binder in 80:20 weight ratio in N-Methyl-2-pyrrolidone (NMP, Sigma-Aldrich) to get a slurry, which was cast either on Al or Cu foils with a doctor blade tool (MTI Corp.). The cathode for Li—O₂ and Li-ion-O₂ cells was prepared by dispersing MWCNTs/FLG 50:50 material and PVDF binder with 80:20 weight ratio in NMP to form a viscous slurry, which was cast onto a GDL (36 BB, Sigracet) using the doctor blade. The anode for Li-ion-O₂ cells was prepared by dispersing Sn@C, SPC, and PVDF binder in a 70:10:20 weight ratio in NMP to achieve a slurry, which was cast on Cu foil. All prepared electrode tapes were dried on a hot plate at 70 °C for 3 h, and cut into discs with diameters of either 10, 14 mm, or 16 mm (geometric area: 0.79, 1.54, and 2.00 cm², respectively). Before transfer to argon-filled glove box (MBraun), all electrodes were further dried under vacuum at 110 °C for 3 h.

2.4. Physical-chemical tests on the electrolytes

Thermogravimetric analysis (TGA) was carried out over the temperature range of 25–1000 °C, under N₂ flow with a heating rate of 5 °C min⁻¹ using a TGA 2 Mettler-Toledo instrument and placing the samples (~8 mg) inside alumina-based pans. Differential scanning calorimetry (DSC) was performed using a DSC250 from TA Instruments. Approximately 5 mg of the electrolyte was hermetically sealed in an aluminum pan inside an Ar-filled glovebox. Initially, the samples were heated to 100 °C with a rate of 5 °C min⁻¹ and held for 5 min. Then, the samples were cooled to -150 °C at a rate of -5 °C min⁻¹ and held for 5 min. Measurements were subsequently taken by heating the samples from -150 °C to 100 °C at a rate of 5 °C min⁻¹. Fourier transform infrared (FT-IR) spectra of solutions were recorded using a Bruker Alpha II spectrometer equipped with an ATR (attenuated total reflection) accessory and a diamond crystal tip. Measurement was conducted inside an Ar-filled glovebox to avoid moisture and oxygen interference. Each

spectrum was collected over a range of 500 cm⁻¹ to 2000 cm⁻¹ with a resolution of 2 cm⁻¹ and with 24 scans per sample. The ATR crystal was cleaned with isopropanol between measurements to prevent cross-contamination. Fourier transform Raman (FT-Raman) spectra were recorded using a Bruker MultiRAM FT-Raman spectrometer equipped with a Nd laser source (1064 nm excitation wavelength). Measurements were performed under ambient conditions. Each spectrum was collected with a laser power of 400 mW, using a spectral range of 500–3500 cm⁻¹. The instrument was configured with a liquid nitrogen-cooled Ge detector. Each sample spectrum was obtained by averaging 100 scans with a resolution of 4 cm⁻¹ to achieve an optimal signal-to-noise ratio. X-ray photoelectron spectroscopy (XPS) measurements were conducted on lithium foils soaked in electrolytes for 48 h in an Ar-filled glovebox to promote SEI film formation. The foils were then dried under vacuum for 24 h to remove residual electrolyte. Sample transfer to the XPS instrument was achieved using a dedicated transfer chamber to prevent atmospheric exposure. Measurements were taken under vacuum using a PHI 5000 VersaProbe III scanning XPS Microprobe, equipped with monochromatic Al K α source at binding energy of 1486.6 eV. Experimental conditions included an X-ray beam size of 100 μm, 25 W power, and an acceleration voltage of 15 kV. Spectra were analyzed using Casa XPS software (version 2.3.26). These several processes were practically hindered by our Li—O₂ cell setup (*i.e.*, top-meshed 2032 coin cell inside sealed glass chambers filled with pure oxygen as described subsequently). However, we are trying to set up an new experimental tool of practical interest to allow the separation of a cycled Li anode from a Li—O₂ sealed cell to perform the related XPS analysis, and the results will be illustrated in future work.

2.5. Electrochemical tests on the electrolytes

All electrochemical tests of the electrolytes were conducted using either CR2032 coin cells (MTI corp.) or T-cells (Swagelok-type, 10 mm-diameter) assembled inside an Ar-filled glovebox (MBraun), where H₂O and O₂ levels were maintained below 0.5 ppm. The ionic conductivity of the solutions was measured through electrochemical impedance spectroscopy (EIS) conducted at various temperatures using stainless-steel | electrolyte | stainless-steel symmetrical coin cell, with an O-ring (23-5FEP-2-50, CS Hyde) having external diameter of 16 mm and internal diameter of 8 mm to hold the solution in place. The O-ring with a thickness of 127 μm enabled to fix the cell constant at 0.0253 cm⁻¹. The EIS spectra were obtained over a frequency range from 100 kHz to 1 kHz using an alternate voltage of 10 mV, while the cell temperature was controlled by a Julabo F12 instrument [37]. The t_+ of the electrolytes was measured using the Bruce-Vincent-Evans method. A chronoamperometric test was carried out by applying 30 mV for 90 min to a symmetrical Li | electrolyte | Li T-cell, where the 2 Li disks with a diameter of 10 mm were separated by 10 glass fiber disks (Whatman GF/A) with diameter of 10 mm soaking the electrolyte. EIS was performed both before and after polarization, using a 10 mV signal over a frequency range from 500 kHz to 100 mHz. The t_+ values were subsequently calculated using Eq. (1):

$$t_+ = \frac{i_{ss}}{i_0} \times \frac{(\Delta V - R_0 i_0)}{(\Delta V - R_{ss} i_{ss})} \quad (1)$$

where i_0 and i_{ss} represent the initial and steady-state current values, respectively; ΔV is the applied voltage; and R_0 and R_{ss} are the interfacial resistance values before and after cell polarization, respectively, as determined through fitting of the impedance spectra (read below for fitting details) [38]. Lithium stripping-deposition tests were conducted at the constant current of 0.1 mA cm⁻² for over 1 h of charge/discharge cycles in a Li | Li symmetrical coin cells, in which a glass fiber separator with diameter of 16 mm (Whatman GF/B), soaked by the electrolyte, separated 2 Li disks with a diameter of 14 mm. Subsequently, the same cells underwent additional stripping-deposition tests, in which charging

and discharging were conducted at constant currents of 0.2 mA cm^{-2} , 0.45 mA cm^{-2} , and 0.8 mA cm^{-2} for 1 h over 24 cycles for each current. The anodic and cathodic regions of the electrochemical stability window were investigated by performing linear sweep voltammetry (LSV) on Li | SPC-Al cell from the open-circuit voltage (OCV) to 5 V vs. Li^+/Li , and cyclic voltammetry (CV) on Li | SPC-Cu cell between 0.01 and 2.0 V vs. Li^+/Li . Both LSV and CV were performed at a scan rate of 0.1 mV s^{-1} in T-cells using carbon electrode and Li disk separated by 2 glass fiber disks (Whatman GF/B) soaking the electrolyte, and an additional Li-reference disk, all with a diameter of 10 mm. The Li/electrolyte interphase resistance during aging was analyzed by performing EIS on symmetrical coin cell using two Li disks with a diameter of 14 mm separated by a glass fiber disk (Whatman GF/B) soaking the electrolyte with a diameter of 16 mm. EIS measurements were conducted over a frequency range from 500 kHz to 100 mHz with a 10 mV alternate voltage signal. Measurements were taken every 20 min during the first hour after cell assembly, hourly for the initial 24 h, and then daily for a duration of 32 days. Each EIS spectrum was fitted to an equivalent circuit model using the non-linear least squares (NLLS) method with the Boukamp software. Only fits with a chi-square (χ^2) of the order of 10^{-4} or lower were considered acceptable for analysis [39,40].

2.6. Electrochemical tests on the Li–O₂ and Li-ion–O₂ cells

The electrochemical tests of Li–O₂ and Li-ion–O₂ cells were carried out using top-meshed CR2032 coin cells (MTI corp.) placed inside sealed glass chambers filled with pure oxygen. The MWCNTs/FLG 50:50 cathode had a diameter of 16 mm, while the anode diameter measured 14 mm, and the two electrodes were separated by two glass fiber disks (Whatman GF/B) with a diameter of 18 mm or 16 mm soaking the electrolyte.

The Li–O₂ cells were cycled at constant current rate of 0.66 mA (0.33 mA cm^{-2}) with cell capacity limited by time to 1 mAh (0.5 mAh cm^{-2}) within a maximum voltage range of 1.5–4.8 V for Li–O₂ using either PEGDME LiTFSI 1 m or PEGDME LiTFSI 1 m LiNO₃ 1 m electrolytes. The Li–O₂ cells have been also subjected to CV within 1.5–4.3 V vs. Li^+/Li potential range using a scan rate of 0.05 mV s^{-1} , and to full discharge/charge test at 100 mA g_{cathode}^{-1} within the 1.8–4.5 V voltage range for 1 cycle. MWCNTs/FLG 50:50 electrodes were retrieved from the above cells at the OCV condition and upon full discharge and full charge, washed with diethylene glycol dimethyl ether (DEGDME, 99 % Sigma Aldrich), and subsequently subjected to *ex-situ* XRD study through a Bruker D8 Advance instrument equipped with a Cu K α radiation source scanning the $30^\circ - 50^\circ 2\theta$ with step size of 0.02° and rate of 10 s step^{-1} .

The Li-ion–O₂ full-cells were assembled using the PEGDME 250 LiTFSI 1 m LiNO₃ 1 m electrolyte, MWCNTs/FLG 50:50 as cathode support, and pre-lithiated Sn@C as anode. Prior to use in Li-ion–O₂ cell, the Sn@C anode was pre-lithiated chemically by *ex-situ* capillary contact of the electrode with a lithium foil for 14 h under a pressure of 120 g cm^{-2} in presence of commercial electrolyte (LP30, Sigma Aldrich battery grade) formed by ethylene carbonate (EC), dimethyl carbonate (DMC) in a 1:1 volume ratio dissolving 1 M of lithium hexafluoro phosphate (LiPF₆). Subsequently the treated anode, indicated as Li_xSn@C, was thoroughly washed with DMC and dried under vacuum. This process ensured the anode to act as the Li-reservoir suitable for Li-ion–O₂ cell application [31]. The Li-ion–O₂ full-cells were cycled at constant current rate of 0.66 mA (0.33 mA cm^{-2}) with cell capacity limited by time to 0.5 mAh (0.25 mAh cm^{-2}) within a maximum voltage range of 0.1–4.8 V. The full-cells were also subjected to galvanodynamic polarization measurement with current increasing from 0 to 6 mA cm^{-2} , using a step of 0.05 mA cm^{-2} for 5 s, subsequent galvanostatic charging to 5 V, EIS tests before and upon the polarization, and further galvanostatic cycling at a current rate of 1, 2, and 3 mA cm^{-2} with voltage ranging from 0 to 5.0 V and charge/discharge time limited to 7.5 min. Furthermore, the Li-ion–O₂ cell has been subjected to a galvanostatic rate capability test by setting 30 min of charge/discharge time, and

varying the current from 0.1, to 0.2 and 0.5 mA cm^{-2} within maximum voltage limit of 4.5 V and minimum of 0.01 V. All electrodes loadings (i. e., mg cm^{-2} of active material) have been indicated in the figure caption of corresponding tests. Cells with the configuration Li | PEGDME 250 LiTFSI 1 m LiNO₃ 1 m | Li_xSn@C have also been assembled under either Ar or O₂ atmospheres, and monitored in terms of potential, EIS, and XRD evolution over 240 h to study the effects of oxygen permeation into the electrolyte. The Li_xSn@C electrodes retrieved from the aged cells were washed with diethylene glycol dimethyl ether (DEGDME, 99 % Sigma Aldrich) before XRD measurements.

2.7. 2.6 Instruments for electrochemical tests

EIS, chronoamperometry, LSV, CV, and galvanodynamic polarization were conducted using a VersaSTAT MC instrument from Princeton Applied Research (PAR-AMETEK), while lithium stripping-deposition and galvanostatic cycling were performed using a MACCOR Series 4000 battery test system.

3. Result and discussion

3.1. Electrolytes physical-chemical characteristics

The physical-chemical characteristics of the electrolytes studied in this work are summarized in Fig. 1 with reference to the PEGDME 250 solvent. Fig. 1a displays the TGA curves (top panels) and corresponding DTG (bottom panels) conducted under an N₂ atmosphere between 25 °C and 1000 °C for pure PEGDME 250 solvent (black), PEGDME 250 LiTFSI 1 m (red), and PEGDME 250 LiTFSI 1 m LiNO₃ 1 m (blue) electrolytes. The comparison reveals significant differences in evaporation kinetics between the pure PEGDME 250 and the electrolytes. Indeed, the solvent begins weight loss at 65 °C and its full evaporation ends at 308 °C, with a DTG peak centered at 270 °C. In contrast, the TGA curve of PEGDME 250 LiTFSI 1 m shows multiple stages of weight loss, starting at 70 °C with an initial DTG peak at 250 °C, mainly attributed to solvent evaporation. The rate of weight loss slows down between 270 °C and 340 °C, likely due to solvent removal from coordination structures formed by the strong interactions between the oxygen groups in the ether-based chain and Li⁺ ions [41,42]. A second significant weight loss occurs at higher temperature until 500 °C, with a DTG peak at 406 °C and residual weight of 1.5 % further decreasing to 0.4 % at 1000 °C. This response corresponds to the degradation of the LiTFSI salt, as confirmed by the TGA of pure LiTFSI in Fig. S1 (Supplementary Material) [43]. Similarly, the TGA curve of PEGDME 250 LiTFSI 1 m LiNO₃ 1 m reveals multiple stages of weight loss beginning at 72 °C, with a DTG peak at 214 °C as the solvent evaporates. Relevantly, the weight loss rate slows down earlier at 240 °C in this solution, due to the higher amount of Li⁺-glyme coordination structures triggered by the concomitant presence of two salts. As observed in the previous sample, a second significant weight loss starts at 370 °C and ends around 500 °C with a residual weight of 2.3 %, further decreasing to 0.65 % at 1000 °C. It is worth mentioning that the degradation of LiNO₃ salt does not occur around 600 °C, as instead expected by the TGA curve of the pure salt in Fig. S1. Rather, LiNO₃ starts degradation over 800 °C due to the above mentioned interaction of Li⁺ with the glyme chains [32], as suggested by the weight loss from 1.7 % to 0.65 % between 800 °C and 1000 °C with slight DTG peak at 870 °C. Fig. 1b shows DSC plots of PEGDME 250 solvent (black, bottom panel), PEGDME 250 LiTFSI 1 m (red, middle panel), and PEGDME 250 LiTFSI 1 m LiNO₃ 1 m (blue, top panel) electrolytes between –150 °C and 100 °C. The DSC plot of pure PEGDME 250 displays an exothermic hump between –74 °C and –63 °C, likely ascribed to crystal reorganization due to the presence of stabilizers such as di-butyl phthalate (DBP) in the commercial glymes, or to other order-disorder rearrangements [44]. Furthermore, the glass transition of the pure solvent may be suggested around –53 °C [45]. A double melting signal is observed between –50 °C and –28 °C with peaks at –43 °C and –35 °C, possibly ascribed

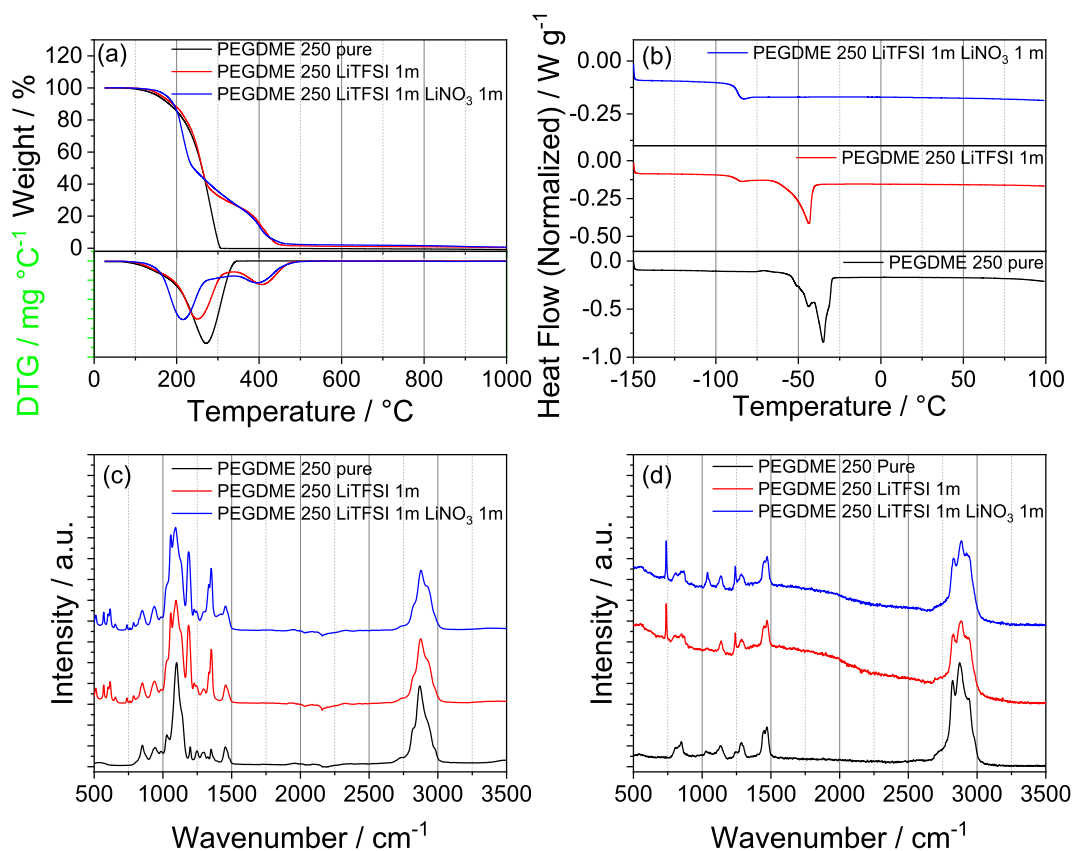


Fig. 1. Physical-chemical characterization of pure PEGDME 250 solvent (black), PEGDME 250 LiTFSI 1 m (red) and PEGDME 250 LiTFSI 1 m LiNO₃ 1 m (blue) electrolytes, in detail: (a) TGA and corresponding DTG curves acquired under N₂ flow between 25 °C and 1000 °C at the 5 °C min⁻¹ rate, (b) DSC thermograms acquired between -150 and 100 °C at 5 °C min⁻¹ rate, and (c) FT-IR and (d) FT-Raman spectra. (For interpretation of the references to colour in this figure legend, the reader is referred to the web version of this article.)

to crystalline heterogeneity promoted by partial melting and reorganization into different structures during the initial thermal treatment of the sample [46]. The DSC of PEGDME 250 LiTFSI 1 m displays a shift of the glass transition down to -88 °C. This shift may be reasonably attributed to an increased amorphous character and flexibility promoted by the above-mentioned interactions between Li⁺ ions and the oxygen atoms in the ether-based chains [47]. In addition, the double melting peak observed for pure PEGDME 250 merges into a single one at -54 °C with a lower magnitude or enthalpy, thus suggesting that LiTFSI can hinder the above mentioned crystalline heterogeneity, and facilitate the electrolyte melting at a lower temperature [44,45]. The DSC of PEGDME 250 LiTFSI 1 m LiNO₃ 1 m shows almost merged peaks for glass transition and melting, and indicates that the two phase changes may occur almost simultaneously between -102 °C and -75 °C. Hence, the glass transition occurs at approximately -90 °C similarly to the LiNO₃-free electrolyte, while the melting substantially shifts to -87 °C and strongly decreases in magnitude likely due to the doubled concentration of Li⁺ ions and the presence of two different anions. Fig. 1c reports the FT-IR spectra of PEGDME 250 solvent (black), PEGDME 250 with LiTFSI 1 m (red), and PEGDME 250 with LiTFSI 1 m and LiNO₃ 1 m (blue). The spectra of the two electrolytes reveal additional peaks compared with PEGDME 250 solvent, all ascribed to the LiTFSI salt: the peak centered at 1351 cm⁻¹ is associated with the asymmetrical stretching of the CF₃ group [48,49], the signal at 1186 cm⁻¹ is due to asymmetrical stretching of the SO₂ group, while the one at 1056 cm⁻¹ is related with asymmetrical stretching of the S-N-S bond [48,50]. Furthermore, the peak at 1133 cm⁻¹ of the SO₂ symmetrical stretching merges with the solvent one at 1025 cm⁻¹. The PEGDME 250 LiTFSI 1 m LiNO₃ 1 m electrolyte shows further peaks at 1420 cm⁻¹ and 827 cm⁻¹ due to asymmetrical stretching and out-of-plane deformation mode of the NO₃⁻ group,

respectively, while the peak at 1300 cm⁻¹ of NO₃⁻ symmetrical stretching merges with the solvent one at 1305 cm⁻¹ [51].

The presence of these peaks suggests actual dissolution of the salts included in the studied electrolytes. Fig. 1d shows the FT-Raman spectra of the electrolytes and the pure solvent, allowing the identification of characteristic features ascribed to each composition. Both electrolytes reveal peaks associated with the LiTFSI salt, such as that centered at 1240 cm⁻¹ due to symmetrical stretching of the -CF₃ group, and at 738 cm⁻¹ due to symmetrical stretching of the S-N-S bond as well as bending of the -CF₃ group [50,52]. In addition, the FT-Raman spectrum of PEGDME 250 LiTFSI 1 m LiNO₃ 1 m shows a peak at 1040 cm⁻¹ due to symmetrical vibration of the NO₃⁻ group, accounting for the salt-solvent interactions [53].

Fig. 2 examines by XPS the composition of the SEI film formed on the surface of lithium foils soaked for 2 days in PEGDME 250 LiTFSI 1 m (red) and PEGDME 250 LiTFSI 1 m LiNO₃ 1 m (blue) electrolytes. The corresponding survey spectra in Fig. 2a highlight a SEI predominantly composed of carbon, oxygen, fluorine, sulfur, nitrogen, and lithium, attributed to degradation and/or precipitation at the metal surface of the electrolytes' components such as PEGDME (mainly C and O) and salts (F, S, N and Li). These outcomes suggest a complex interaction of the electrolytes with the lithium leading to SEI formation. Deconvoluted XPS spectra presented in Figs. 2b-g provide detailed insights on SEI composition by identifying the contributions of individual elements. The C 1s spectra (Fig. 2b) display peaks at 293.5 eV corresponding to the -CF₃ group, at 287.4 eV associated with Li₂CO₃ [54-56], and at approximately 285 eV due to -C-C- bonds [24]. Relevantly, the peak at 286 eV linked with R-O-R and R-O-Li bonds [56] is observed only in the sample containing LiNO₃ salt, thus suggesting the latter to partially limit the solvent degradation from ether to carbonate at the lithium surface.

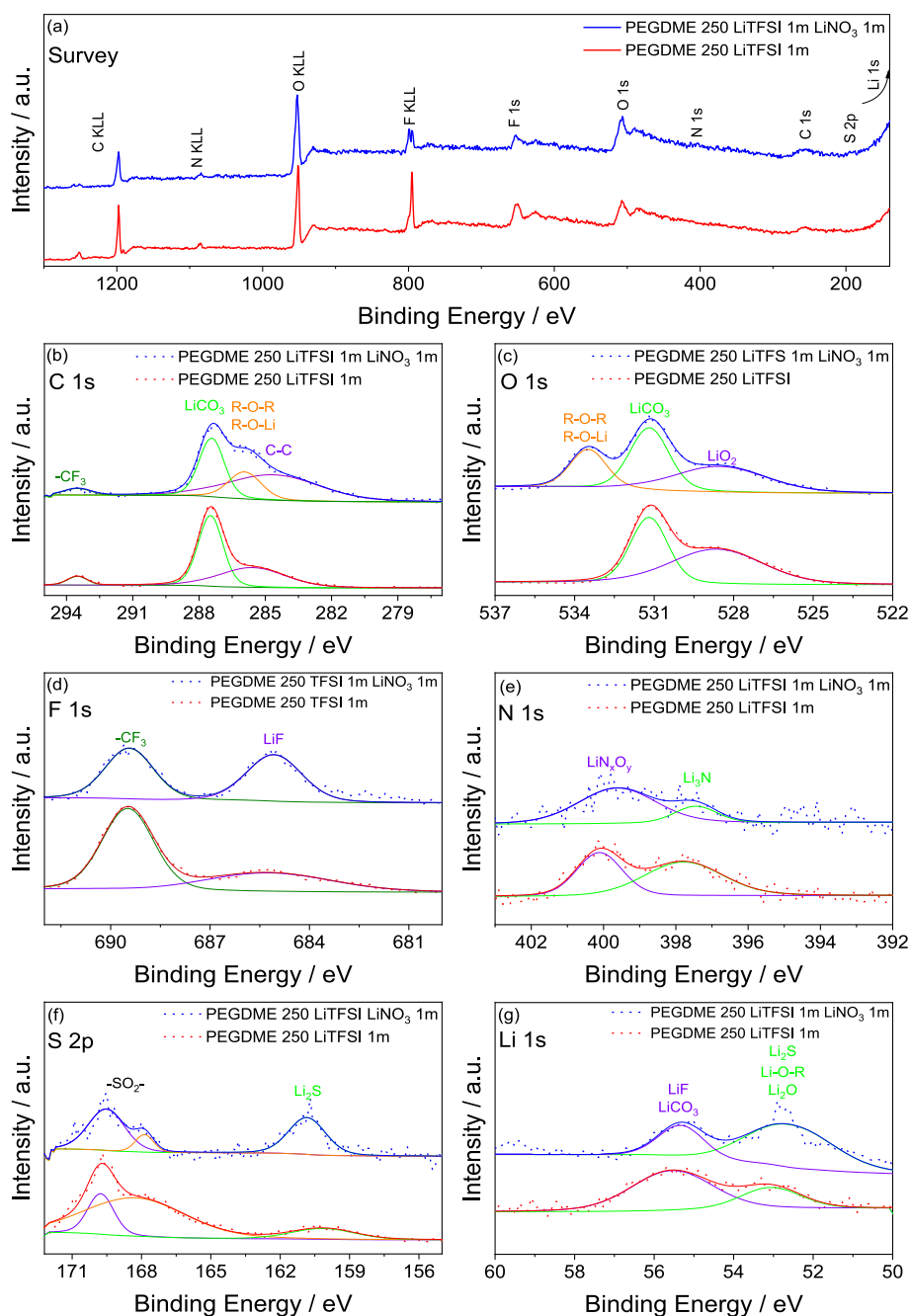


Fig. 2. XPS characterization of the SEI, in detail: (a) survey spectra of the surface of lithium metal foils soaked in PEGDME 250 LiTFSI 1 m (red) PEGDME 250 LiTFSI 1 m LiNO₃ 1 m (blue) electrolytes for 2 days, and deconvoluted spectra of (b) C 1s, (c) O 1s, (d) F 1s, (e) N 1s, (f) S 2p and (g) Li 1s core levels. (For interpretation of the references to colour in this figure legend, the reader is referred to the web version of this article.)

Analogously, the O 1s spectra (Fig. 2c) reveal a peak at 533.6 eV of R-O-R and R-O-Li only for the sample containing LiNO₃, consistently with the results of the C 1s spectra [56]. On the other hand, peaks respectively at 531.2 eV and 528.5 eV in the O 1s spectra indicate the presence of Li₂CO₃ and Li₂O in the SEI for both electrolytes [24,32,57]. The F 1s spectra (Fig. 2d) include a peak at 689.4 eV related with the -CF₃ group in line with the C 1s identification [58], and another one at 685.1 eV associated with LiF [32,59] likely formed by LiTFSI decomposition at the lithium surface. The convoluted N 1s signal (Fig. 2e) reveals two distinct peaks, the first at 397.4 eV ascribed to negatively charged nitrogen species such as Li₃N (N³⁻) [24], and the second at 399.7 eV attributed to various nitrogen-oxygen compounds (LiN_xO_y) [58,60]. The latter peak is more pronounced in the spectrum of the LiNO₃-added

electrolyte, as indeed expected by the additional nitrogen source of the sacrificial agent, whereas the nitrogen contributions in the other electrolyte originate only from the LiTFSI. The two peaks at 169.4 eV and 167.9 eV in the S 2p spectra (Fig. 2f) can be attributed to the S 2p_{3/2} and S 2p_{1/2} doublet of the -SO₂- group, while the one at ~161 eV corresponds to Li₂S, all peaks suggesting the degradation of the LiTFSI salt [61,62]. The Li 1s spectra (Fig. 2g) feature a peak at approximately 53 eV, which can be attributed to Li₂O, Li-O-R, and Li₂S species, more relevantly in the electrolyte containing LiNO₃ that stabilizes Li-O-R species as mentioned above [57,58]. Additionally, a peak at 55.5 eV is observed, and possibly associated with Li₂O and Li₂CO₃ species [63]. The XPS results highlight that the SEI is predominantly composed of inorganic species, shaped by the decomposition products of the

electrolytes and their interactions with lithium. On the other hand, the addition of LiNO_3 favors the presence of organic species such as R-O-R and Li-O-R, mainly due to the concomitant side chemical reduction or precipitation of this sacrificial salt at the lithium metal interphase which relevantly modifies the SEI layer composition. This process ultimately contributes to a better stability of the lithium interface, thus suggesting the significant role of LiNO_3 in the SEI.

3.2. Electrochemical features of the electrolytes and the lithium interphases

Fig. 3 summarizes the electrochemical characteristics of the electrolytes investigated by means of various techniques. The conductivity plots over the temperature achieved by EIS are shown in Fig. 3a, while the corresponding Nyquist plots are presented in Fig. S2 (Supplementary Material). The PEGDME 250 LiTFSI 1 m has a conductivity of $1.91 \times 10^{-3} \text{ S cm}^{-1}$ at 84.7°C , which is higher compared to that of PEGDME 250 LiTFSI 1 m LiNO_3 1 m at the same temperature ($1.55 \times 10^{-3} \text{ S cm}^{-1}$). Cooling down leads to conductivity decrease in the former electrolyte, whereas the conductivity of the latter one remains almost constant, and the two solutions reach the same value of $1.5 \times 10^{-3} \text{ S cm}^{-1}$ at 70.5°C . Beyond this point, the conductivity of the electrolyte

containing LiTFSI only progressively decreases to reach $1.34 \times 10^{-4} \text{ S cm}^{-1}$ at -7.4°C , instead the electrolyte containing both LiTFSI and LiNO_3 exhibits a slight increase to $1.71 \times 10^{-3} \text{ S cm}^{-1}$ at 57.7°C and a subsequent gradual decrease until $3.69 \times 10^{-4} \text{ S cm}^{-1}$ at -7.4°C . Notably, the conductivity of the electrolyte containing the two salts remains always higher than that of PEGDME LiTFSI 1 m below 70.5°C . It is worth mentioning that the conductivity plot of PEGDME 250 LiTFSI 1 m can be adequately described by Arrhenius-type behavior, whereas the electrolyte added by LiNO_3 requires the application of the Vogel–Tamman–Fulcher (VTF) theory to explain the conductivity trend [37,38,43,64]. The electrolytes are subsequently examined in symmetrical Li | Li cell to determine t^+ using the Bruce–Vincent–Evans method [38]. Table 1 reports the calculated t^+ values and summarizes all the parameters used for calculation, while the chronoamperometric curves and the Nyquist plots from corresponding EIS measurements are presented in Fig. S3 (Supplementary Material). The achieved values for the LiNO_3 -free solution ($t^+ = 0.58$) and LiNO_3 -added one ($t^+ = 0.59$) differ only within the experimental error range (Fig. 3a inset), thus suggesting that the presence of NO_3^- does not reduce the current transported by Li^+ expected by the equation $t^+ = \frac{q^+}{\sum_i q^i}$, where q^+ represents the charge carried by Li^+ , where q^i is the one carried by all the ions, that is, Li^+ ,

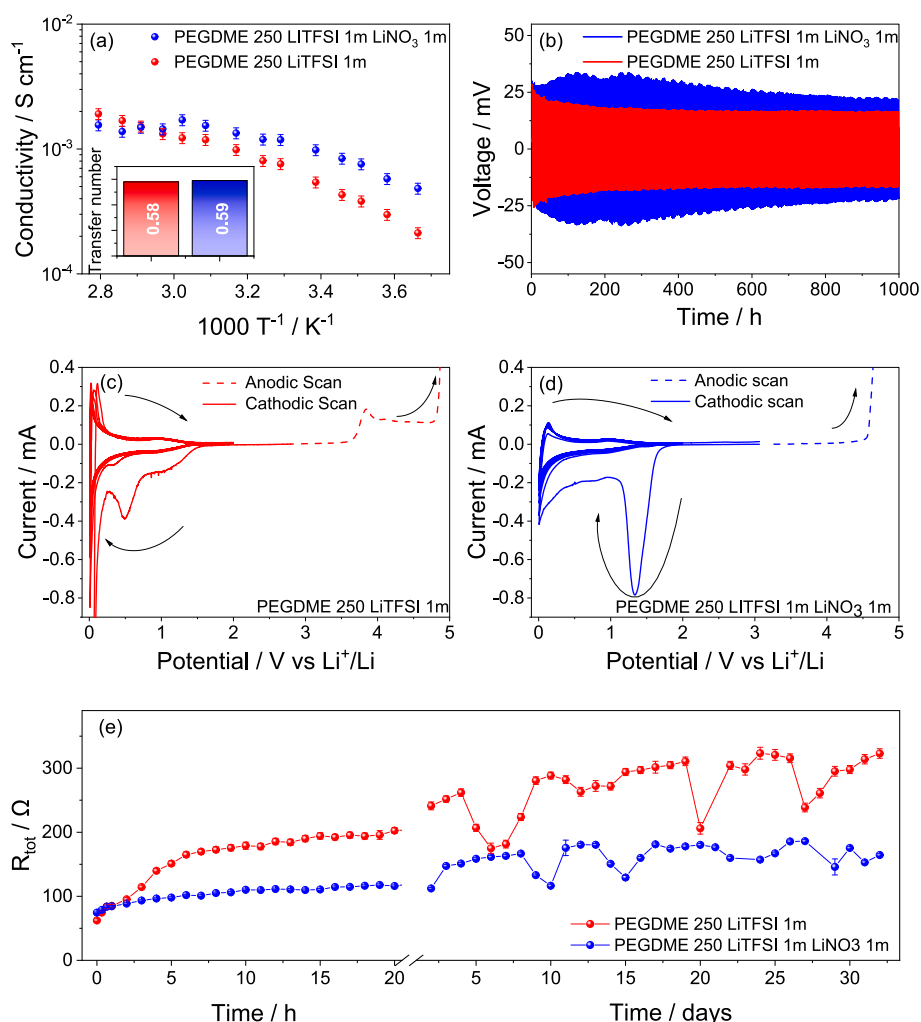


Fig. 3. Electrochemical characterization of PEGDME 250 LiTFSI 1 m (red) and PEGDME 250 LiTFSI 1 m LiNO_3 1 m (blue) electrolytes, in detail: (a) conductivity trends vs. temperature and t^+ values (inset), (b) lithium stripping/deposition test performed on Li | Li symmetrical cells, by applying a current of 0.1 mA cm^{-2} , step time 1 h, (c, d) electrochemical stability window determined by means of CV in the cathodic region (solid line) and LSV in the anodic one (dashed line) in lithium cells with (c) PEGDME 250 LiTFSI 1 m, and (d) PEGDME 250 LiTFSI 1 m LiNO_3 1 m, using SPC-Cu working electrode from 0.01 V to 2 V vs. Li^+/Li for the cathodic region, and SPC-Al working electrode from OCV to 5 V vs. Li^+/Li for the anodic region at a scan rate of 0.1 mV s^{-1} , (e) trends of the interphase resistance vs. time related to Li | Li cells. (For interpretation of the references to colour in this figure legend, the reader is referred to the web version of this article.)

Table 1

Parameters used in eq. (1) according to Bruce-Vincent-Evans method to calculate t^+ of electrolytes. See Fig. S3 (Supplementary Material) for chronopotentiometric curve and Nyquist plots.

Electrolyte	i_0 (mA)	i_{ss} (mA)	R_0 (Ω)	R_{ss} (Ω)	t^+
PEGDME 250 LiTFSI 1 m	0.082	0.065	181	143	0.58
PEGDME 250 LiTFSI 1 m LiNO ₃ 1 m	0.064	0.042	107	104	0.59

NO₃⁻, and TFSI⁻ in the solution containing LiNO₃, or excursively by Li⁺ and TFSI⁻ in the bare solution. Likely, this issue is avoided in this work since the LiNO₃ mainly precipitates from the electrolyte bulk to the electrode surface to form the protective SEI layer, thus holding similar t^+ values for the two electrolytes, and possibly analogue ionic conductivity and viscosity. Furthermore, the t_+ values are consistent with those reported for other glyme-type electrolytes, indicating these solutions as suitable candidates for application in lithium batteries [16,32]. The electrochemical stability of the electrolytes is evaluated in Fig. 3b by conducting prolonged lithium stripping and deposition experiments through galvanostatic cycling using a current of 0.1 mA cm⁻² in symmetrical Li | Li configuration. The cell with PEGDME 250 LiTFSI 1 m electrolyte (red) shows polarization decrease from an initial value of 28.8 mV to 16.5 mV during the initial 500 h of cycling, and subsequent stabilization upon 1000 h of test. This trend suggests a consolidation of the SEI layer, resulting in steady performance over extended cycling. The cell using PEGDME 250 LiTFSI 1 m LiNO₃ 1 m solution has initial polarization of 30 mV, *i.e.*, slightly higher value compared to the LiNO₃-free electrolyte, which decreases to 28.1 mV and fluctuates by increasing to 33.1 mV before dropping to 30.5 mV, further rising to 33.7 mV and stabilizing at 22.1 mV after approximately 900 h. These fluctuations can be attributed to partial dissolution, growth, and subsequent stabilization of the SEI layer, as promoted by the presence of LiNO₃ in this electrolyte which may actually trigger the SEI formation dynamics. Furthermore, the higher polarization observed for the cell containing LiNO₃-added solution may be associated with the more complex SEI composition, as already suggested by XPS analysis. On the other hand, a more robust and protective SEI could in principle improve the long-term stability of the cell and prevent possible dendrite formation at the lithium metal surface. The electrochemical stability window is investigated in lithium cells with SPC working electrode both for PEGDME 250 LiTFSI 1 m electrolyte (Fig. 3c) and PEGDME 250 LiTFSI 1 m LiNO₃ 1 m electrolyte (Fig. 3d) using LSV for the anodic region and CV for the cathodic one (see experimental section for details). The LSV of PEGDME 250 LiTFSI 1 m solution reveals an initial peak at 3.8 V vs. Li⁺/Li, attributed to possible oxidation of PEGDME 250 stabilizer (DBP) already mentioned during DSC discussion. Subsequently, a main peak starting at 4.8 V vs. Li⁺/Li indicates the ultimate degradation of the electrolyte through oxidative decomposition, *i.e.*, a value which is considered the anodic stability limit. The CV of the same electrolyte in Fig. 3c shows during the first cathodic scan a broad reductive wave around 1 V vs. Li⁺/Li likely due to Li-insertion into the disordered CSP matrix [65,66], a peak at 0.5 V vs. Li⁺/Li ascribed to the irreversible reduction of the electrolyte with SEI formation [67,68], and the typical sharp signal near 0 V vs. Li⁺/Li due to the beginning of lithium plating onto the working electrode [69]. The subsequent anodic scan reveals a peak at ~0.1 V vs. Li⁺/Li due to the dissolution of previously plated Li by stripping from the electrode surface [69], and a small peak at around 1 V vs. Li⁺/Li ascribed to Li de-insertion from the carbonaceous matrix [65]. During the 2nd cycle the reduction peak at 0.5 V vs. Li⁺/Li decreases, and it vanishes during the subsequent cycles suggesting the gradual consolidation of a protective SEI layer that avoids further electrolyte degradation. In addition, the other mentioned peaks reversibly evolve with slight shift and a lower magnitude. Hence, these data indicate that the PEGDME 250 LiTFSI 1 m electrolyte has an electrochemical stability window extending from 0 V

to 4.8 V vs. Li⁺/Li, with a side degradation at ~3.8 V vs. Li⁺/Li which could potentially affect the cell performance unless a favorable SEI is formed. The LSV of the cell using the PEGDME 250 LiTFSI 1 m LiNO₃ 1 m electrolyte (Fig. 3d) reveals that the peak attributed to DBP oxidation almost disappears, thus suggesting its possible direct reaction with LiNO₃ which deactivates the related anodic signal. The main anodic peak is observed at 4.6 V vs. Li⁺/Li, indicating a lower onset of oxidative decomposition of the LiNO₃-added electrolyte compared with the PEGDME 250 LiTFSI 1 m one. Whilst lowering the oxidative decomposition potential might initially appear detrimental, it is important to point out that LiNO₃ is intentionally added to the electrolyte as a sacrificial agent which decomposes preferentially to facilitate the formation of a robust and effective SEI, ultimately improving the overall stability and of the cell [70]. On the other hand, the missing irreversible oxidation at 3.8 V Li⁺/Li represents a further, non negligible, advantage of the LiNO₃-added solution. The CV in Fig. 3d shows a distinct peak at 1.3 V vs. Li⁺/Li during the first cathodic scan with PEGDME 250 LiTFSI 1 m LiNO₃ 1 m electrolyte, which is attributed to the irreversible reduction of the sacrificial additive [70,71]. The broad wave from 1.1 to 0.2 V vs. Li⁺/Li observed by further lowering the potential includes partial reduction of the electrolyte and Li insertion into the amorphous SPC [67,68]. The last cathodic peak at ~0 V vs. Li⁺/Li consists with the above-mentioned Li deposition, however with less extent compared to the LiNO₃-free electrolyte due to the formation of more resistive SEI [16,65,69]. During the subsequent anodic scan, a peak is observed at approximately 0.1 V vs. Li⁺/Li as the Li strips away from the electrode, and a small signal appears around 1 V vs. Li⁺/Li due to Li de-insertion from SPC [65,66]. Interestingly, the electrolyte degradation peaks disappear already at the second cathodic scan, and the CV proceeds only with reversible Li (de)insertion at ~1 V and stripping/deposition at ~0 V vs. Li⁺/Li, without significant shift. This outcome suggests the formation of fully passivating SEI already during the initial cycle, which is achieved only after the 2nd one in the LiNO₃-free electrolyte. The chemical stability of the electrolyte in contact with metallic Li is evaluated by monitoring the time evolution of electrode/electrolyte inter-phase resistance in symmetrical cells. The resistance value plotted vs. time in Fig. 3e are achieved through NLLS fitting of the corresponding EIS spectra in Fig. S4 with results in Tables S1-S4 (Supplementary Material). The EIS response of PEGDME 250 LiTFSI 1 m electrolyte is modelled using the R_e(R₁Q₁)(R₂Q₂)(R₃Q₃) equivalent circuit, including the electrolyte resistance (R_e) at high frequency, and a series of resistances with constant phase elements (R_iQ_i) reflecting the complexity of the interfacial processes, where SEI and charge transference locate at medium frequencies while diffusion occurs at low frequency. The total resistance sharply increases from an initial value of 62.2 Ω to 165 Ω upon six hours, which suggests significant changes at the electrode/electrolyte interface as the SEI begins formation. A more gradual, whilst continuous, resistance growth is observed subsequently with values reaching 213 Ω after 24 h, 241 Ω upon 2 days, and 322 Ω over the whole test of 32 days. Occasional fluctuations with minor resistance decrease are attributed to partial dissolution, reorganization or morphology changes of the SEI layer into a dynamic process extending over time, and possibly leading to final electrode/electrolyte interface stabilization. Instead, the EIS data of the cells with the PEGDME 250 LiTFSI 1 m LiNO₃ 1 m electrolyte are more accurately modelled using the simpler R_e(R₁Q₁)(R₂Q₂) equivalent circuit, suggesting a different interfacial structure and SEI formation kinetics. The cell displays a resistance of 74.5 Ω at the OCV that reaches 93.5 Ω after six hours, 124 Ω after 24 h, and 147 Ω upon 72 h, *i.e.*, relevantly lower values compared to the LiNO₃-free solution.

The resistance rises further by aging but at a slower rate, reaching 164 Ω by the end of the test after 32 days. The more stable resistance trend, the lower overall values, and the simpler equivalent circuit for the PEGDME 250 LiTFSI 1 m LiNO₃ 1 m electrolyte compared to the LiNO₃-free one indicate the formation of a SEI of superior quality. Hence, the presence of LiNO₃ enhances the stability and uniformity of the SEI layer,

which in turn contributes to the improved cell performance.

3.3. The lithium oxygen cells

Fig. 4 reports the galvanostatic cycling under O_2 atmosphere of the two electrolytes in cells using MWCNTs/FLG 50:50 as cathode support [15] and Li metal as anode. The voltage profile of the Li– O_2 cell with the PEGDME 250 LiTFSI 1 m electrolyte (Fig. 4a) reveals during the first cycle the discharge shape of the ORR taking place between 2.6 V and 2.4 V, while the charge process foresees the OER between 4.3 V and 4.7 V. The cell demonstrates an initial polarization ranging from 1.4 to 1.8 V during charge and from 0.3 to 0.5 V during discharge, based on the theoretical potential of 2.9 V vs Li^+/Li for the redox reaction between lithium and oxygen to form lithium peroxide (Li_2O_2) [11,12]. It is worth mentioning that the charge/discharge time is controlled to achieve a capacity limited to 0.5 $mAh\ cm^{-2}$, corresponding to specific value of approximately 500 $mAh\ g^{-1}$ as referred to the MWCNTs/FLG 50:50 material weight in the electrode (geometrical area 2 cm^2). This setup is typically adopted in Li– O_2 cells to avoid excessive deposition of Li_2O_2 into a highly insulating layer, that can in turn remarkably hinder the reversibility of the electrochemical process [16,32]. During the initial stages the cell experiences an increase of polarization, accompanied by coulombic efficiency decrease from the 10th to the 14th cycle, and subsequent increase until the 20th cycle as evidenced by the

corresponding trend in Fig. 4b. The cell stabilizes after 20 cycles, and the coulombic efficiency holds a value approaching 100 % within a relevant steady state condition until the 50th cycle. This behavior can be attributed to ohmic effects on the cell polarization promoted by the initial growth, partial dissolution, and subsequent consolidation of the SEI layer at the lithium metal anode, as already observed during the EIS and CV measurement. According to the current value and the capacity limit used in this test (i.e., 0.33 $mA\ cm^{-2}$, and 0.5 $mAh\ cm^{-2}$, respectively), the lithium contribution to the overall polarization is estimated to be of the order of 0.2 V, as demonstrated by the stripping/deposition tests at various capacity and current regimes reported in Fig. S5 (Supplementary Material). Furthermore, a favorable structural reorganization of the OER/ORR products at the cathode surface suggested by previous works can contribute to the cell stabilization observed from the 20th until the 50th cycle [14,32,33]. After the 50th cycle, the charge polarization increases and the voltage reaches the upper limit of 4.8 V by the 60th cycle, which prevents complete OER. However, the subsequent discharge is not hindered, since the cell configuration still allows the deposition of Li_2O_2 at the electrode surface according to the capacity limit, with consequent fluctuation of the coulombic efficiency until the 90th cycle. Nevertheless, the efficiency fluctuation increases the cell polarization during discharge, which evolves at 2 V at the 90th cycle. The first voltage profile of the Li– O_2 cell using the electrolyte supplemented with $LiNO_3$ (Fig. 4c) exhibits a discharge process occurring

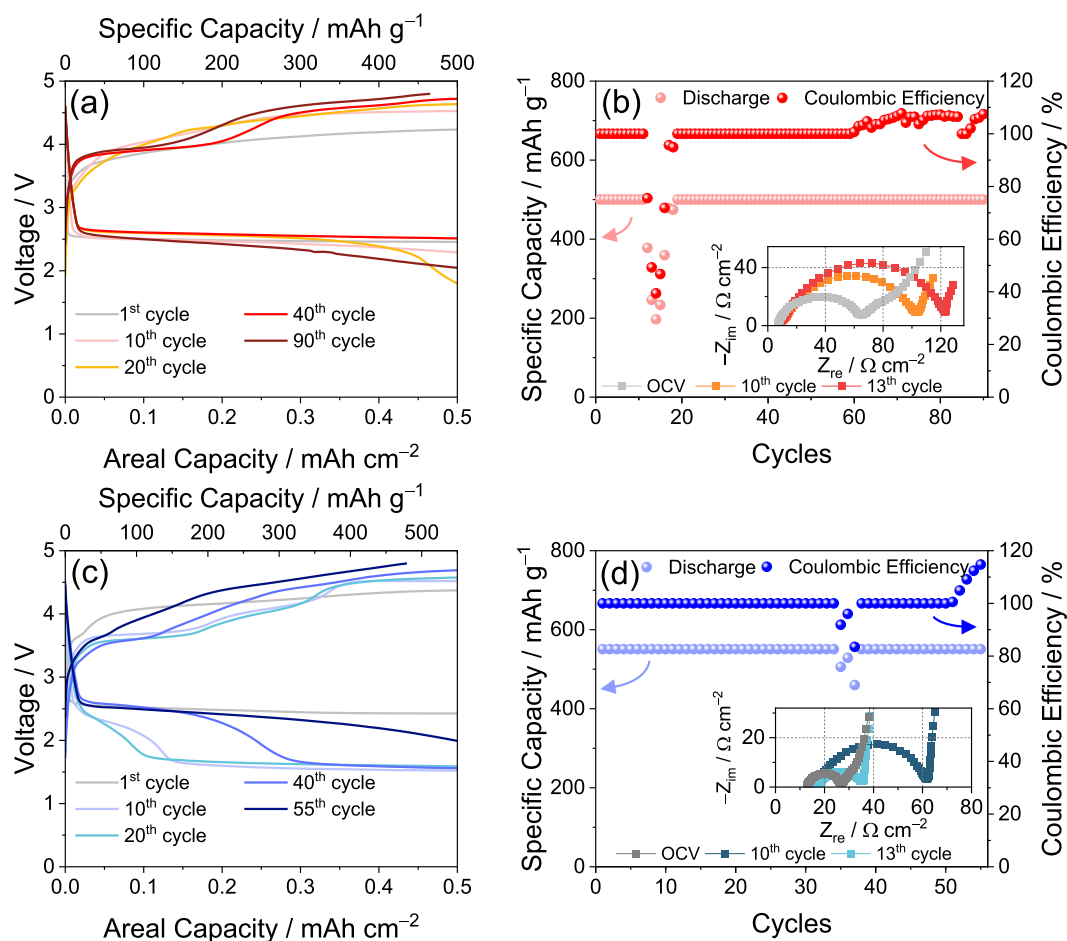


Fig. 4. Voltage profile and cycling trends, respectively, of galvanostatic measurement of Li– O_2 cells using either (a, b) PEGDME 250 LiTFSI 1 m (red) or (c, d) PEGDME 250 LiTFSI 1 m $LiNO_3$ 1 m (blue) as electrolyte, and MWCNTs/FLG 50:50 as cathode support. The insets of panels b and d report the Nyquist plots of the EIS performed on the corresponding cells at the OCV and after the 10th and 13th galvanostatic run (cell recovered at the charge state). Constant current: 0.66 mA. Maximum voltage range: 1.5–4.8 V. Capacity limited to 0.5 $mAh\ cm^{-2}$. Cathode geometric area: 2.0 cm^2 , loading: $1.0 \pm 0.1\ mg\ cm^{-2}$ of MWCNTs/FLG 50:50. EIS performed using an AC signal amplitude of 10 mV with frequency ranging from 500 kHz to 100 mHz. (For interpretation of the references to colour in this figure legend, the reader is referred to the web version of this article.)

between 2.6 V and 2.4 V and a charge process taking place between 4.0 V and 4.4 V. These values account for an initial polarization ranging from 0.3 to 0.5 V in the ORR, and from 1.1 to 1.5 V in the OER, with a specific capacity of 550 mAh g^{-1} as referred to the cathodic material mass. As the cycling proceeds, the discharge voltage shifts down to 1.5 V while the charge one rises up to 4.5 V at the 10th cycle. This trend leads to a significant increase of polarization, which appears notably higher compared to the cell using the LiNO_3 -free electrolyte, as likely attributed to the irreversible reduction of the sacrificial agent by the initial stages of the test where the SEI forms and stabilizes. At the 20th cycle the voltage shape is similar to the previous one, instead the profiles at the 40th and 55th cycles are different, since the discharge gradually raises back to 2.0 V and the charge shifts up to reach the 4.8 V cutoff. Analogously to the cell using the bare electrolyte, reaching the charge cutoff avoids the complete OER, whilst the ORR occurs until the capacity limit (0.5 mAh cm^{-2}), thus leading to a coulombic efficiency exceeding 100 % (Fig. 4d). Conversely, the occasional efficiency decrease below 100 % observed in Fig. 4d between the 34th and 38th cycles indicates that the OER occurs according to the capacity limit, while the ORR partially evolves as limited by the voltage cutoff. The reasons for the different trend of the efficiency during the initial cycles of the cells of Fig. 4b and Fig. 4d, have been investigated by EIS measurements performed at the OCV and after the 10th and 13th galvanostatic cycles. The related Nyquist plots, reported in the corresponding figure as inset, evidence that the cell using the LiNO_3 -added electrolyte has a lower resistance than that using the bare Li electrolyte both at the OCV and after cycling, with values ranging from 19 to 45Ω for the former and from 107 to 129Ω for the latter, as calculated in Table 2 and Table 3 exploiting the $R_e(RQ)Q_w$ equivalent circuit. These outcomes justify in part the different efficiency trends in the two cells, and suggest the interphase stabilizing role of the LiNO_3 additive. Furthermore, the data suggest a more complex behavior of the LiNO_3 additive in oxygen atmosphere rather than the one experienced upon CV/EIS in cells using the electrolytes under Ar. Hence, the SEI in Li-O_2 cells may be subjected to partial dissolution and subsequent re-formation promoted by direct reaction of O_2 permeated into the electrolyte with the LiNO_3 reduction products. These changes may actually affect the Li-O_2 cell polarization, and account for the profiles observed in Fig. 4c,d. On the other hand, the use of LiNO_3 in the electrolyte can promote a stable interphase with the anode and remarkably avoid dendrite formation, which are preferential characteristics of choice for cells operating in an open environment such the lithium-air battery.

A further insight on the Li-O_2 cells reaction mechanism is given by Fig. 5. The CV curves performed within a potential ranging from 1.5 to 4.3 V vs. Li^+/Li show for both bare solution (Fig. 5a) and LiNO_3 -added one (Fig. 5b) the occurrence of the ORR during the cathodic scans, with peak centered below 2.5 V vs. Li^+/Li . Furthermore, the cell using the LiNO_3 -added electrolyte evidences an additional current onset below 1.6 V vs. Li^+/Li ascribed to the beginning of LiNO_3 reduction process already discussed in Fig. 3d, as well as a wider ORR peak compared to the bare solution which indicates slightly different reaction kinetics promoted by the sacrificial additive. On the other hand, the subsequent anodic scan shows the currents associated to the OER, occurring through a first step at 3.5 V vs Li^+/Li and a second one above 3.8 V vs Li^+/Li , in

Table 2

NLLS analysis carried out on the Nyquist plots reported as inset of Fig. 4b. The impedance spectra were acquired on a $\text{Li} \mid \text{PEGDME 250 LiTFSI 1 m} \mid \text{MWCNTs:FLG, O}_2$ cell at the OCV and after the 10th and 13th galvanostatic run (cell recovered at the charge state), and fitted using the Boukamp software, by exclusively accepting results with χ^2 values of the order of 10^{-4} .

Condition	Equivalent circuit	R	χ^2
OCV	$R_e(RQ)Q_w$	107.3 ± 2.8	2×10^{-4}
After 10th cycle	$R_e(RQ)Q_w$	115.2 ± 2.1	1×10^{-4}
After 13th cycle	$R_e(RQ)Q_w$	129.1 ± 4.4	2×10^{-4}

Table 3

NLLS analysis carried out on the Nyquist plots reported as inset of Fig. 4d. The impedance spectra were acquired on a $\text{Li} \mid \text{PEGDME 250 LiTFSI 1 m} \mid \text{LiNO}_3 \text{ 1 m} \mid \text{MWCNTs:FLG, O}_2$ cell, at the OCV and after the 10th and 13th galvanostatic run (cell recovered at the charge state), and fitted using the Boukamp software, by exclusively accepting results with χ^2 values of the order of 10^{-4} .

Condition	Equivalent circuit	R	χ^2
OCV	$R_e(RQ)Q_w$	25.4 ± 0.5	4×10^{-4}
After 10th cycle	$R_e(RQ)Q_w$	45.2 ± 0.8	4×10^{-4}
After 13th cycle	$R_e(RQ)Q_w$	19.7 ± 0.4	2×10^{-4}

agreement with the galvanostatic profiles of Fig. 4 and with literature work [14]. The oxidation peaks width, intensity and distribution appear different for the two cells, thus suggesting different kinetics also for the OER. The actual formation of Li_2O_2 , and possibly Li_2O , during ORR and their dissolution by OER, are demonstrated by the galvanostatic cycling tests of the Li-O_2 cells in the voltage range from 1.8 to 4.5 V, coupled with *ex-situ* XRD of the MWCNTs/FLG 50:50 cathode retrieved from the cells. The related voltage profiles show a relevant reversible capacity of $\sim 2000 \text{ mAh g}^{-1}$ for the bare solution (*i.e.*, 2.2 mAh cm^{-2} in Fig. 5b) and of $\sim 4500 \text{ mAh g}^{-1}$ for the LiNO_3 -added one (*i.e.*, 5.4 mAh cm^{-2} in Fig. 5c). These high values of capacity, particularly for the cell using the LiNO_3 additive, are achieved herein since a wide voltage range is used for cycling to enhance the XRD signals of the electrode in the subsequent investigation, which is a condition typically avoided in the case of repeated cycling tests to promote the cell life as mentioned above. Therefore, the electrodes are collected from cells at the OCV condition, after a full discharge, and upon subsequent charge, and the related XRD patterns are reported in Fig. 5e for the bare electrolyte and in Fig. 5f for the LiNO_3 -added solution. The diffraction patterns depict the appearance of the main peaks associated to Li_2O_2 at $2\theta = 32.8^\circ$ and 35° (ICSD # 24143) upon discharge, and their full vanishing after charge in both electrolytes, thus confirming the reversibility of the ORR/OER already suggested by the high efficiency of the related cells. Furthermore, the appearance of a side peak at 2θ of 36.7° indicate for the cell using the bare electrolyte a slightly diverse reaction pathway that may lead to Li_2O traces (ICSD # 108886) due to the different kinetics observed above, or a characteristics SEI due to reactivity between the electrode and the electrolyte at the 3-sides interphase [72]. These outcomes once again evidence the potentiality of the cell setup exploited herein, and possibly suggest a more adequate interphase for the LiNO_3 -added electrolyte due to the absence of side signals in the XRD patterns, and the high reversibility of the electrochemical process observed in Fig. 5.

3.4. The metal-free Li-ion oxygen cell

Fig. 6 reports the voltage profiles and cyclic trends of the two electrolytes in a Li-ion- O_2 configuration, using a nanostructured Sn@C anode studied in our previous work [35]. The anode contains 40 wt% of Sn and 60 % of carbon, and can deliver a capacity ranging from 300 mAh g^{-1} to 600 mAh g^{-1} depending on the c-rate, with a characteristic voltage signature mainly evolving below 0.6 V [35]. Before use in full-cell, the anode is pre-lithiated chemically as previously described [31], through capillary contact with lithium metal to achieve a $\text{Li}_x\text{Sn@C}$ electrode which can act as the lithium reservoir to allow the ORR. Fig. 6a,b shows the voltage profile and cycling trends of the $\text{Li}_x\text{Sn@C} \mid \text{PEGDME 250 LiTFSI 1 m} \mid \text{MWCNTs/FLG 50:50, O}_2$ Li-ion cell cycled with capacity limited to 0.25 mAh cm^{-2} , corresponding to a specific value of $\sim 350 \text{ mAh g}^{-1}$ as normalized to the MWCNTs/FLG 50:50 weight in the electrode. During the first discharge, the ORR occurs between 2.3 V and 1.7 V, which is a lower range than the one observed in the Li-O_2 cell using the same electrolyte, as expected by the higher potential of the Li-Sn alloying (*i.e.*, from 0.2 to 0.5 V) [73] compared to Li metal stripping/deposition (*i.e.*, 30 mV at low current in Fig. 2 and $\sim 100 \text{ mV}$ at higher current in Fig. S5). The charge voltage profile reflects

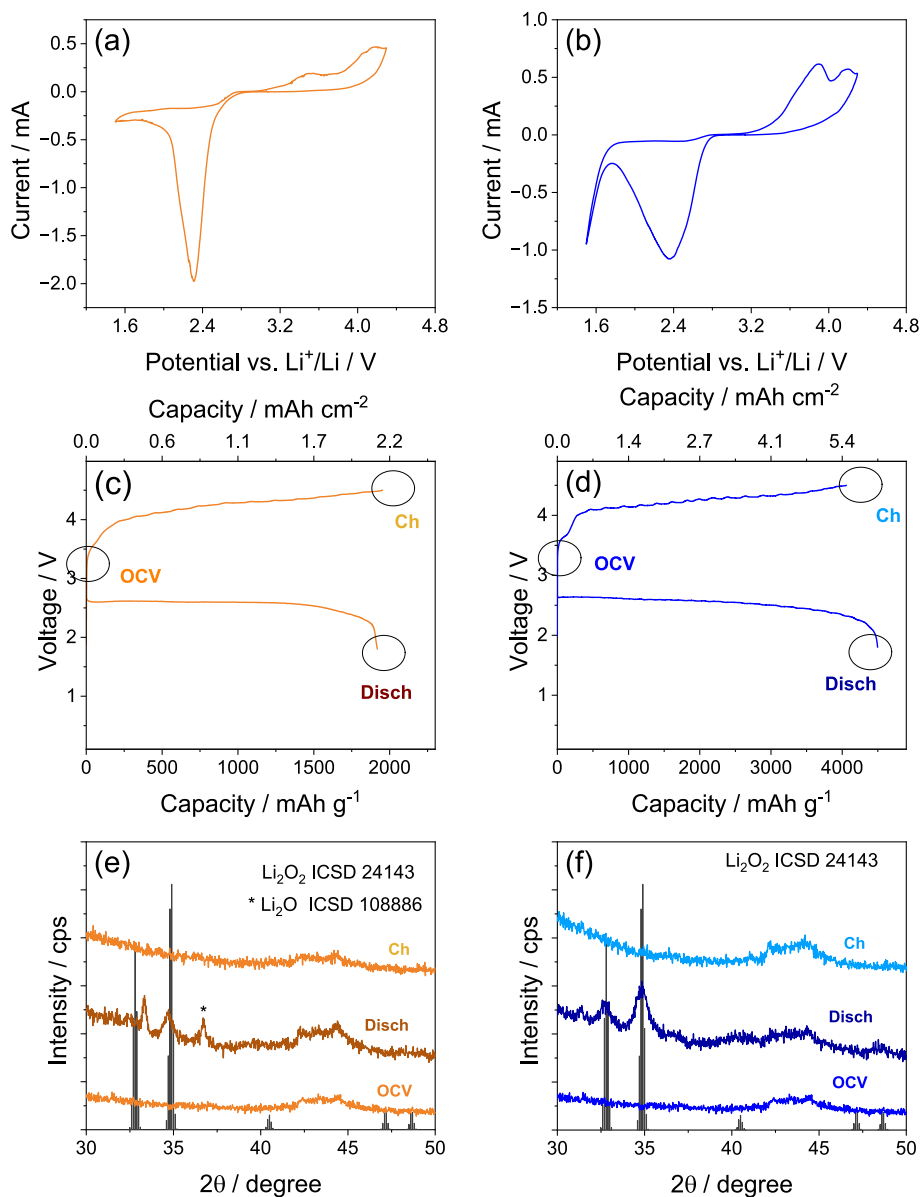


Fig. 5. Investigation of Li–O₂ cells using either (a, c, e) PEGDME 250 LiTFSI 1 m (orange scale) or (b, d, f) PEGDME 250 LiTFSI 1 m LiNO₃ 1 m (blue scale) as electrolyte, and MWCNTs/FLG 50:50 as cathode support. In detail: (a, b) CV profiles between 1.5 and 4.3 V vs. Li⁺/Li at scan rate of 0.05 mV s⁻¹; (c, d) voltage profile of full discharge/charge tests between 1.8 and 4.5 V at a current of 100 mA g⁻¹ of MWCNTs/FLG 50:50. Cathode geometric area: 2.0 cm², loading: 1.2 ± 0.1 mg cm⁻² of MWCNTs/FLG 50:50; (e, f) XRD patterns of the MWCNTs/FLG 50:50 cathode extracted from the cell at the OCV, after discharge and after subsequent charge indicated by circles in panels (c) and (d), with ICDS references of Li₂O₂ (# 24143) and Li₂O (# 108886). (For interpretation of the references to colour in this figure legend, the reader is referred to the web version of this article.)

OER between 2.7 V and 4.2 V, in line with profile and range expected by the combination of the voltage shapes ascribed with Li–O₂ cell charge and Li–Sn de-alloying [15,73]. Subsequently, both charge and discharge voltages drop down, due to oxygen permeation into the electrolyte, migration from the cathode and direct reaction with the Li_xSn@C anode. This process decreases the alloying degree in the anode by subtracting lithium, thus increasing its potential and lowering the overall voltage of the Li-ion-O₂ cell [72]. After three cycles the ORR becomes limited by potential cutoff (0.5 V) rather than time, and the discharge capacity decreases, as shown in the selected cycles in Fig. 6a (10th, 20th, and 40th cycles), instead the charge holds the capacity limit of 0.25 mAh cm⁻². The above described voltage fluctuation affects the cell efficiency (Fig. 6b) which decreases below 100 % at the 4th cycle, reaches about 84 % at the 10th cycle, and holds this value for 25 cycles. Subsequently, the efficiency rises back to reach 100 % at the 30th cycle,

and decreases again to reach 70 % at the 40th cycle. The same figure shows that the cell delivers an initial discharge specific capacity of 350 mAh g⁻¹, which is retained for the 71 % in 40 cycles, despite the above described efficiency fluctuation. Analogously, Fig. 6c,d presents the voltage profile and cycling trends of the Li_xSn@C | PEGDME 250 LiTFSI 1 m LiNO₃ | MWCNTs/FLG 50:50, Li-ion-O₂ cell cycled with capacity limited to 0.25 mAh cm⁻², corresponding to a specific value of ~275 mAh g⁻¹. The first discharge of this cell reveals ORR between 2.2 V and 1.1 V, which is a lower range than that observed in the Li–O₂ cell and the Li-ion-O₂ cell without LiNO₃ salt. Meanwhile, the OER during charging takes place between 3.1 V and 4.3 V, leading to higher polarization compared to the LiNO₃-free electrolyte. During the subsequent cycles, the ORR/OER voltage gradually shifts for the above discussed oxygen permeation, however with a slower rate compared to the cell using the bare solution (compare Fig. 6a and Fig. 6c). Therefore, the cell

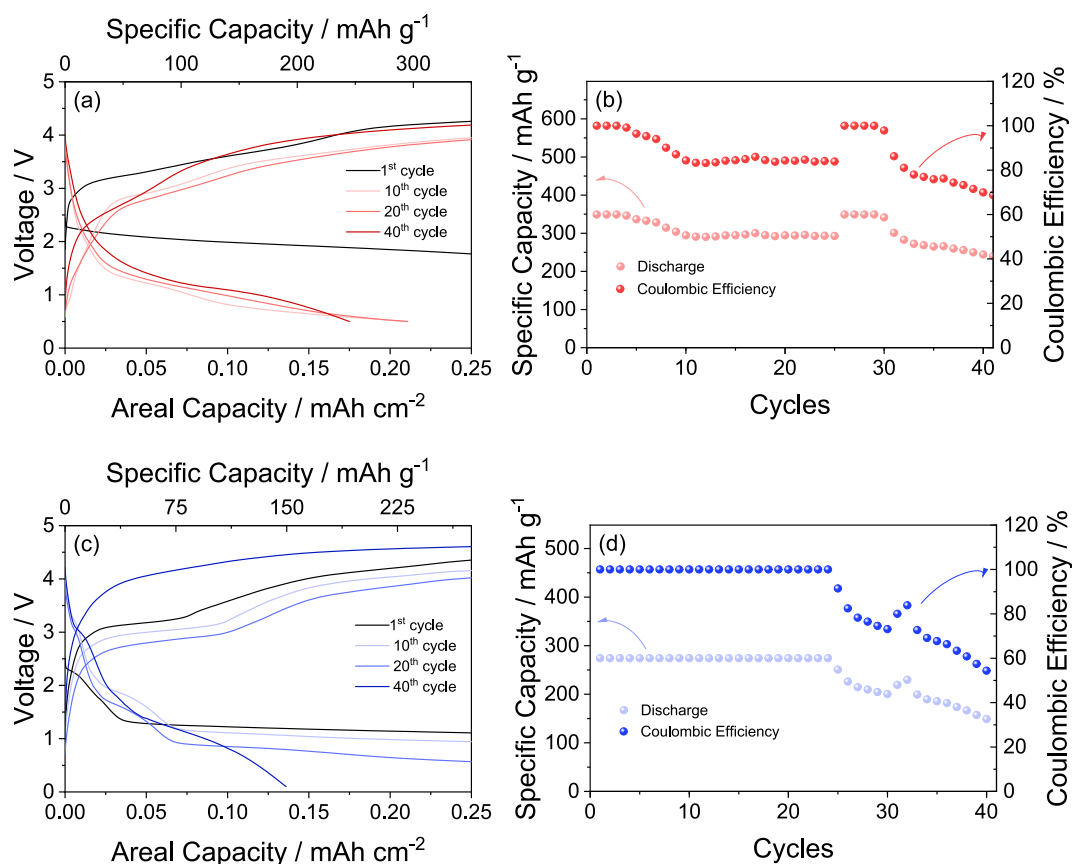


Fig. 6. Voltage profile and cycling trends, respectively, of galvanostatic measurement of Li-ion-O₂ cells using either (a, b) PEGDME 250 LiTFSI 1 m (red) or (c, d) PEGDME 250 LiTFSI 1 m LiNO₃ 1 m (blue) as electrolyte, MWCNTs/FLG 50:50 as cathode support and pre-lithiated Sn@C (Li_xSn@C) as anode. Constant current: 0.66 mA. Maximum voltage range: 0.5–4.8 V for PEGDME 250 LiTFSI 1 m and 0.1–4.8 V for PEGDME 250 LiTFSI 1 m LiNO₃ 1 m cells. Capacity limited to 0.25 mAh cm⁻². Cathode geometric area: 2.0 cm², loading: 0.8 ± 0.1 mg cm⁻² of MWCNTs/FLG 50:50. Anode geometric area 1.54 cm², loading: 5.9 ± 0.1 mg cm⁻² of Sn@C. (For interpretation of the references to colour in this figure legend, the reader is referred to the web version of this article.)

using the LiNO₃-added solution reaches the discharge cutoff upon 25 cycles, after which the efficiency decreases below 100 % and the discharge capacity below the 275 mAh g⁻¹ limit (Fig. 6d). It is worth noting that the cell using the electrolyte with LiNO₃ can hold the initial efficiency of 100 % much longer than the one using the bare electrolyte (compare Fig. 6b and Fig. 6d). This behavior accounts for a favorable effect of the additive, which can enhance the film formation at the electrode surface and partially limit the issue ascribed to the direct reaction of the permeated oxygen with the Li-alloying anode. However, after 25 cycles cell capacity and efficiency decrease to reach respectively 150 mAh g⁻¹ and 54 % at the 40th cycle. Although, the cell containing the electrolyte with LiNO₃ initially demonstrates a more stable voltage profile and higher efficiency, the cell with the bare solution exhibits a higher capacity retention and final efficiency after the 40 cycles taken into account. As already demonstrated by a previous work [72], and above discussed in Fig. 4, the oxygen permeation into the electrolyte, subsequent migration from the cathode, and its direct reaction with the Li_xSn@C anode decreases the alloying degree in the latter electrode by subtracting lithium, thus increasing its potential and lowering the overall voltage of the Li-ion-O₂ cell. This process leads to the final capacity drop observed in Fig. 6, which is more relevant when the anode is more deeply employed and the overall cell capacity increased as demonstrated hereafter.

Despite preliminary, these proof-of-concept cells show that both electrolytes may be suitable media for Li-ion-O₂ configuration due their stability within the operating voltage range. It is worth mentioning that several strategies have been proposed to enable the use of the alloying anodes in Li-ion-O₂ cells, including the employment of protective film

for the anode, the use of *ad hoc* designed additives, or of different anode materials with higher stability in this reactive environment [74]. Previous literature reports on the metal free, Li-ion oxygen cell were limited to less than 15 charge/discharge cycles, in addition using more volatile electrolytes [31,72]. To further stress the novelty of our cell, Fig. 7 shows the practical evaluation of the Li-ion-O₂ cell using the PEGDME 250 LiTFSI 1 m LiNO₃ 1 m electrolyte, *i.e.*, the one with the better performances according to our findings with the MWCNTs/FLG 50:50 cathode and the Li_xSn@C as anode, by exploiting polarization tests, EIS, and galvanostatic cycling at increasing current rates. The Fig. 7a shows the polarization curves until a current as high as 6 mA cm⁻², repeated for three times upon galvanostatic charge of the full cell after each test. The first polarization curve (dark blue) reveals two main plateaus, a shorter one centered at 2 V with a power peak of 2 W g⁻¹, and a longer one evolving from 1.5 to lower voltages involving a higher power of 3 W g⁻¹. After the first polarization test, the cell is charged again (voltage profile in Fig. 7b), verified by EIS to have a small resistance from 10 to ~20 Ω (figure inset and Table 4), and subjected to a second polarization run within the same condition as for the previous one. Surprisingly, the polarization curve changes shape (Fig. 7a, blue), the first region at voltages over 2 V extends, and the second one below 2 V shrinks, thus triggering a higher power peak at about 4 W g⁻¹. These modifications, as well as a similar shape observed upon third test within the same conditions, indicate the stability of the Li-ion oxygen cell and its remarkable power. It is worth mentioning that this good behavior may be triggered by favorable interfacial modifications upon cycling, and by the presence of the LiNO₃ which may act as a redox mediator in the low voltage region [75]. The relevant performance of this Li-ion-O₂ full-cell is further

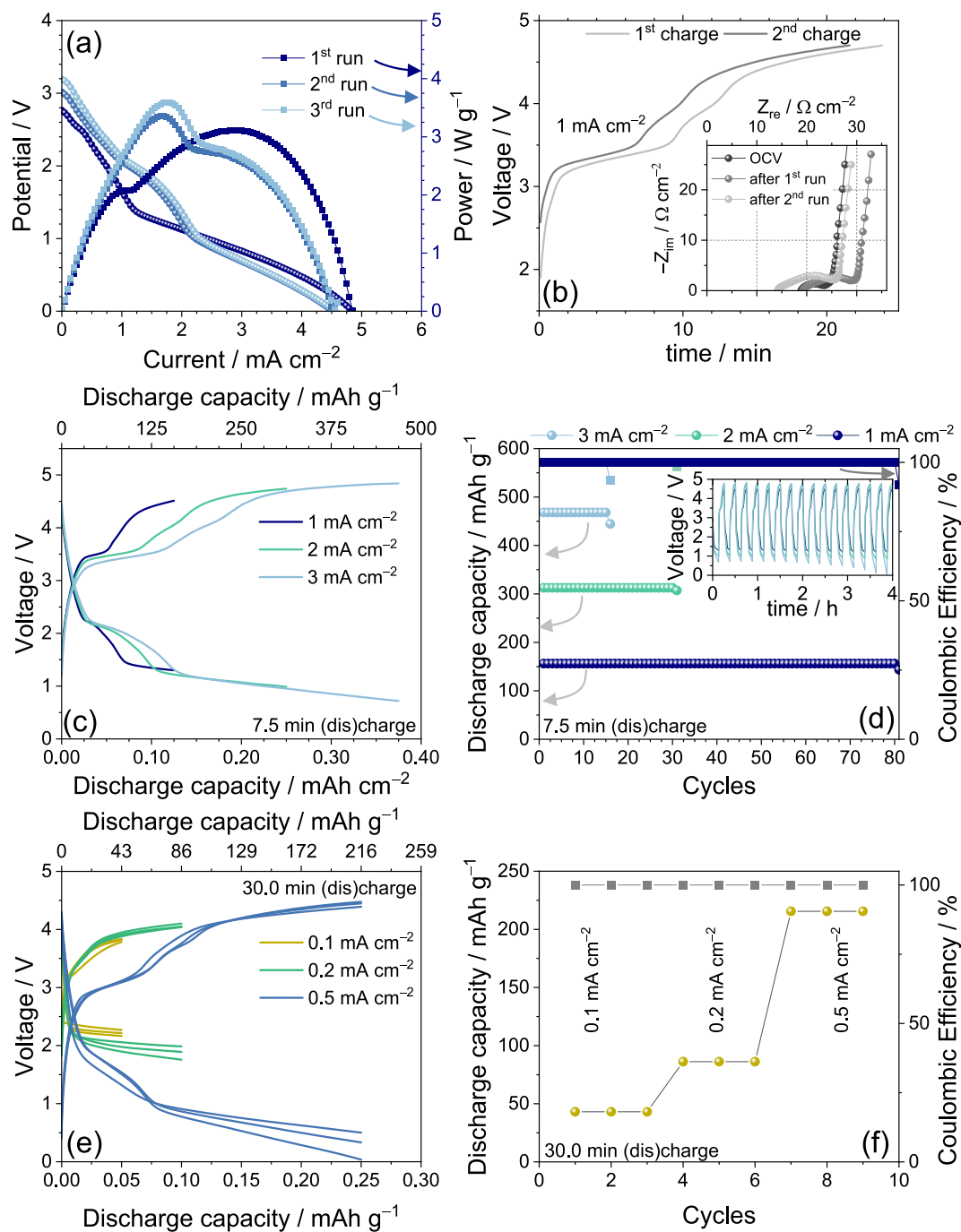


Fig. 7. Practical evaluation of Li-ion-O₂ battery using the PEGDME 250 LiTFSI 1 m LiNO₃ 1 m electrolyte, MWCNTs/FLG 50:50 as cathode support, and pre-lithiated Li_xSn@C as anode: (a) polarization plot (repeated for three times on the same full-cell) obtained by means of galvanodynamic polarization measurement (current range 0–6 mA cm⁻², step: 0.05 mA cm⁻², 5 s), (b) voltage profile of the galvanostatic charge occurred after the 1st and 2nd polarization run (Nyquist plot acquired on the full-cell, collected before and upon the polarization, are reported as inset), (c) 2nd voltage profile of three Li-ion-O₂ full-cells investigated by applying a current rate of 1, 2, and 3 mA cm⁻² for 7.5 min, and (d) corresponding discharge capacity trends vs. cycle number (coulombic efficiency in right-hand side y-axis, inset shows the voltage profiles vs. time trends), (e) voltage profiles and (f) corresponding capacity trends vs. cycle number of a rate capability test of Li-ion-O₂ full-cell by applying a current of 0.1, 0.3, and 0.5 mA cm⁻² for 30 min, voltage range: 0–5.0 V, cathode geometric area: 2.0 cm², loading: 1.0 ± 0.2 mg cm⁻² of MWCNTs/FLG 50:50, anode geometric area: 1.54 cm², loading: 6.4 ± 0.2 mg cm⁻² of Sn@C. Test performed at 25 °C.

demonstrated by galvanostatic cycling tests performed by applying current rates increasing from 1 to 3 mA cm⁻², and a constant time limit to increase concomitantly delivered capacity and power (see experimental section). The Fig. 7c shows a steady state voltage signature (2nd cycle) similar to the one discussed in Fig. 6c, however with a higher polarization as expected by the ohmic drop promoted by the much higher current. On the other hand, the corresponding cycling trends in

Fig. 7d evidence a remarkable stability for the cell at 1 mA cm⁻², which delivers a capacity of 150 mAh g⁻¹ for 80 cycles with efficiency of 100 %, before losing the performance. Relevant, however with a shorter cycle life, are the cells cycled at 2 and 3 mA cm⁻², which deliver 300 and 450 mAh g⁻¹ for 30 and 15 cycles, respectively, due to the more demanding anode exploitation mentioned above. Despite the cycle life is still shortened by reaction of the O₂ diffused into the electrolyte with the

Table 4

NLLS analysis carried out on the Nyquist plots reported as inset of Fig. 7b. The impedance spectra were acquired on a $\text{Li}_x\text{Sn@C} \mid \text{PEGDME 250 LiTFSI 1 m LiNO}_3 \text{ 1 m} \mid \text{MWCNTs:FLG, O}_2$ full-cell, at the OCV and after the first and second galvanodynamic polarization runs, and fitted using the Boukamp software, by exclusively accepting results with χ^2 values of the order of 10^{-4} or lower.

Condition	Equivalent circuit	R	χ^2
OCV	$R_e(RQ)Q_w$	10.1 ± 0.3	2×10^{-5}
After 1 st run	$R_e(RQ)Q_w$	18.7 ± 0.4	3×10^{-5}
After 2nd run	$R_e(RQ)Q_w$	22.3 ± 1.5	3×10^{-4}

lithiated anode, the improved performances reported herein for the Li-ion version of the oxygen cell indicate the system as very promising and safe battery for next generation energy storage applications. Another rate capability test is subsequently performed by increasing the discharge/charge time to 30 min and ranging the current from 0.1 to 0.5 mA cm^{-2} , to exploit the lower polarization region and reduce the voltage gap of the cell using PEGDME 250 LiTFSI 1 m LiNO_3 1 m electrolyte. The voltage profiles of Fig. 7e indicate that the cell operates by holding the discharge plateau over 2.2 V with specific capacity of 43 mAh g^{-1} , and energy density of 95 Wh kg^{-1} at 0.1 mA cm^{-2} , whilst the working voltage is 2 V with specific capacity of 86 mAh g^{-1} and energy density of 172 Wh kg^{-1} at 0.2 mA cm^{-2} , over 3 repeated cycles (Fig. 7f). Instead, the cell cycled at 0.5 mA cm^{-2} operates similarly to those cycled at 1, 2 and 3 mA cm^{-2} (compare Fig. 7e and Fig. 7c), within a wide voltage ranging from 0.5 to 4.5 V, with a specific capacity of 216 mAh g^{-1} and average energy of $\sim 500 \text{ Wh kg}^{-1}$. Despite the significant polarization at the higher currents, the performances of the Li-ion oxygen cell reported in this work match the ones of the typical Li-ion battery, however without using metals at the cathode side with a very low economic impact. The above mentioned direct reaction of the $\text{Li}_x\text{Sn@C}$ anode with oxygen permeated into the electrolyte is demonstrated by Fig. S6 (Supplementary Material). Indeed, the OCV potential evolutions for lithium cells exploiting the configuration $\text{Li} \mid \text{PEGDME 250 LiTFSI 1 m LiNO}_3 \text{ 1 m} \mid \text{Li}_x\text{Sn@C}$ under Ar (black line) or O_2 (blue line) atmosphere reported in Fig. S6a reveal a steady state value of 0.45 V vs. Li^+/Li for the former, while a continuous change accounting for $\text{Li}_x\text{Sn@C}$ dealloying process prolonged for 240 h for the latter. The potential modification of the cell under O_2 without any current flow certainly confirms the direct reaction of the lithiated Sn@C with the oxygen permeated into the electrolyte (*i.e.*, a *short-circuit-like* reaction). This direct reaction leads also to the growth of a passivation oxide layer which covers the anode material and depresses the XRD diffraction of the residual, non lithiated Sn@C as evidenced by the XRD patterns of the electrodes recovered from the aged cells in Fig. S6b.

This issue is also evidenced by the EIS evolution of the two interphases with Nyquist plots of the two cells at the beginning of the test (Fig. S6c) and upon 240 h of aging (Fig. S6d) in Ar (black) and O_2 (blue) environments. The plots reveal for both cells an increase of the impedance as promoted by the SEI growth, however with a more remarkable magnitude for the latter cell (under O_2 R_{tot} increases from 60 to 698 Ω) than the former (under Ar R_{tot} increases from 169 to 517 Ω), in addition with change of the related equivalent circuit (see Table S5 in Supplementary Material, where R_{tot} of the interphase is represented by $R_1 + R_2$). We would mention that this drawback may be mitigated as above mentioned by anode protection using membranes, artificial SEIs, or other additives in the electrode interphase [74].

4. Conclusion

This study evaluated the thermal, chemical, electrochemical, and interfacial properties of PEGDME-based electrolytes with LiTFSI and LiNO_3 salts, and proposed their possible use in Li-O_2 battery. TGA and DSC revealed that LiTFSI and LiNO_3 significantly influence the thermal behavior, glass transition trend, and melting point of the PEGDME 250.

The data demonstrated that PEGDME 250 LiTFSI 1 m is stable over 200 $^\circ\text{C}$, whereas the addition of LiNO_3 lowers the glass transition temperature from -53 to -88 $^\circ\text{C}$, and reduces the melting enthalpy, while FT-IR and FT-Raman confirmed the characteristic contribution of the electrolyte components. XPS at the solid state highlighted the influence of LiNO_3 in modifying the SEI composition and improving the stability of the lithium interface. The PEGDME 250 LiTFSI 1 m LiNO_3 1 m electrolyte exhibited better conductivity at temperatures below 61 $^\circ\text{C}$ compared to PEGDME 250 LiTFSI 1 m, while the latter electrolyte demonstrated superior value at higher temperatures. The conductivity trend of PEGDME 250 LiTFSI 1 m over temperature exhibited Arrhenius-type behavior, instead the PEGDME 250 LiTFSI 1 m LiNO_3 1 m required the VTF theory, while the electrolytes revealed almost the same t_+ value of 0.6 suggesting only minor effect of LiNO_3 in the Li^+ transport. Lithium stripping-deposition tests demonstrated extended stability, with lower polarization PEGDME 250 LiTFSI 1 m LiNO_3 compared with PEGDME 250 LiTFSI 1 m. LSV and CV indicated that the PEGDME 250 LiTFSI 1 m solution has a stability window ranging from 0 V to 4.8 V vs. Li^+/Li , and a side oxidation at 3.8 V vs. Li^+/Li due to the presence of DBP additive in the glyme. Instead, the solution with LiNO_3 revealed stability from 0 V to 4.6 V vs. Li^+/Li , beyond which decomposition occurs without any trace of the above side reaction at lower voltage. Li-stripping/deposition tests have shown polarization less than 30 mV upon 1000 h, while the Li/electrolyte interphase revealed a resistance below 150 Ω for the LiNO_3 added solution and above 300 Ω for the bare one upon 32 days of aging, thus suggesting the additive to promote a stable SEI. The addition of LiNO_3 to the electrolyte solution lowered its full decomposition from 4.8 V vs. Li^+/Li to 4.6 V vs. Li^+/Li , but it also avoided the side oxidation at 3.8 V vs. Li^+/Li , thus promoting the cell stability and decreasing the SEI resistance. On the other hand, the polarization of the Li-O_2 half-cell cell increased and the coulombic efficiency varied during the initial stages due to ohmic effects promoted by initial growth of the SEI and partial LiNO_3 precipitation. The cell subsequently stabilized, and the coulombic efficiency approached 100 % at the steady-state more relevantly for the LiNO_3 added solution than the bare one, thus suggesting an enhanced SEI using the former electrolyte rather than the latter despite the resistive character. The Li-O_2 cell operated even without LiNO_3 addition in the electrolyte at capacity limited to 0.5 mAh cm^{-2} ($\sim 500 \text{ mAh g}^{-1}$), however it achieved better performance using the LiNO_3 -added solution without capacity limited. Indeed, Li-O_2 cells operating within voltage ranging from 1.5 to 4.5 V, without any capacity limit, delivered $\sim 2000 \text{ mAh g}^{-1}$ with the bare solution (*i.e.*, 2.2 mAh cm^{-2}) and of $\sim 4500 \text{ mAh g}^{-1}$ with the LiNO_3 -added one (*i.e.*, 5.4 mAh cm^{-2}). Interestingly, *ex-situ* XRD confirmed for both cells formation and dissolution of Li_2O_2 during ORR/OER. Overall, the tests in Li-O_2 half-cells indicated smaller initial polarization for the bare electrolyte, whilst better interfacial characteristics with lower resistance for the LiNO_3 -added one, thus suggesting the latter solution for preferential use in Li-ion- O_2 cell in which the lithium metal has been replaced by a $\text{Li}_x\text{Sn@C}$ alloying anode. The results demonstrated that the full-cell can deliver at 2 V a power density as high as 4 W g^{-1} , a capacity of 150 mAh g^{-1} for 80 cycles with efficiency of 100 % at 1 mA cm^{-2} , and a relevant capacity of 300 and 450 mAh g^{-1} for 30 and 15 cycles at 2 and 3 mA cm^{-2} , respectively. These results suggested the setup used herein as suitable for environmentally compatible, safe, and low cost energy storage application.

CRedit authorship contribution statement

Stanislav Levchenko: Writing – original draft, Visualization, Methodology, Investigation, Formal analysis, Data curation, Conceptualization. **Edoardo Barcaro:** Writing – original draft, Visualization, Methodology, Investigation, Formal analysis, Data curation, Conceptualization. **Alessio Comini:** Visualization, Investigation, Formal analysis. **Aleksandar Matic:** Visualization, Supervision, Resources, Data curation. **Jusef Hassoun:** Writing – review & editing, Writing – original

draft, Visualization, Validation, Supervision, Software, Resources, Project administration, Methodology, Investigation, Funding acquisition, Formal analysis, Data curation, Conceptualization.

Declaration of competing interest

The authors declare that they have no known competing financial interests or personal relationships that could have appeared to influence the work reported in this paper.

Acknowledgements

This work was funded under the National Recovery and Resilience Plan (NRRP), Mission 04 Component 2 Investment 1.5 – NextGenerationEU, Call for tender n. 3277 dated December 30, 2021, Award Number: 0001052 dated June 23, 2022. The work was also performed within the grant “Fondo di Ateneo per la Ricerca Scientifica, FAR 2024”, University of Ferrara, and the project “Accordo di Collaborazione Quadro 2015” between University of Ferrara (Department of Chemical and Pharmaceutical Sciences) and Sapienza University of Rome (Department of Chemistry). The authors thank the company BeDimensional S.p.A., Lungotorrente Secca 30R, Genova, 16163, Italy, for providing FLG powder used in the electrode composition.

Appendix A. Supplementary data

Supplementary data to this article can be found online at <https://doi.org/10.1016/j.jcis.2025.139622>.

Data availability

Data will be made available on request.

References

- J.B. Skjærseth, Towards a European green Deal: the evolution of EU climate and energy policy mixes, *Int. Environ. Agreements* 21 (2021) 25–41, <https://doi.org/10.1007/s10784-021-09529-4>.
- G. Goppelt, Electrification by 2030 - the OEMs' plans, *ATZelectronics worldwide* 17 (2022) 36–41, <https://doi.org/10.1007/s38314-022-0825-x>.
- J. Piątek, T.M. Budnyak, S. Monti, G. Barcaro, R. Gueret, E.S. Grape, A. Jaworski, A. K. Inge, B.V.M. Rodrigues, A. Slabon, Toward Sustainable Li-Ion Battery Recycling: Green Metal-Organic Framework as a Molecular Sieve for the Selective Separation of Cobalt and Nickel, *ACS Sustain. Chem. Eng.* 9 (2021) 9770–9778, <https://doi.org/10.1021/acssuschemeng.1c02146>.
- S. Link, L. Schneider, A. Stephan, L. Weymann, P. Plötz, Feasibility of meeting future battery demand via domestic cell production in Europe, *Nat. Energy* 10 (2025) 526–534, <https://doi.org/10.1038/s41560-025-01722-y>.
- R.E. Ciez, J.F. Whitacre, Examining different recycling processes for lithium-ion batteries, *Nat. Sustainability* 2 (2019) 148–156, <https://doi.org/10.1038/s41893-019-0222-5>.
- K. Turcheniuk, D. Bondarev, V. Singhal, G. Yushin, Ten years left to redesign lithium-ion batteries, *Nature* 559 (2018) 467–470, <https://doi.org/10.1038/d41586-018-05752-3>.
- X. Bai, Y. Sun, X. Li, R. He, Z. Liu, J. Pan, J. Zhang, A deep dive into spent Lithium-ion batteries: from degradation diagnostics to sustainable material recovery, *Electrochem. Energy Rev.* 7 (2024) 33, <https://doi.org/10.1007/s41918-024-00231-y>.
- Y. Li, J. Lu, Metal-Air Batteries: Will They Be the Future Electrochemical Energy Storage Device of Choice? *ACS Energy Lett.* 2 (2017) 1370–1377, <https://doi.org/10.1021/acseenergylett.7b00119>.
- Md.A. Rahman, X. Wang, C. Wenz, High energy density metal-air batteries: a review, *J. Electrochem. Soc.* 160 (2013) A1759–A1771, <https://doi.org/10.1149/2.062310jes>.
- J. Hassoun, K. Kimura, Y. Tominaga, Cellulose-based electrolytes in rechargeable Zn-battery: an overview, *Adv. Sustainable Syst.* (2025), <https://doi.org/10.1002/advsu.202500287>.
- L. Carbone, S.G. Greenbaum, J. Hassoun, Lithium sulfur and lithium oxygen batteries: new frontiers of sustainable energy storage, *sustain, Energy Fuel* 1 (2017) 228–247, <https://doi.org/10.1039/c6se00124f>.
- C.O. Laoire, S. Mukerjee, K.M. Abraham, E.J. Plichta, M.A. Hendrickson, Elucidating the mechanism of oxygen reduction for lithium-air battery applications, *J. Phys. Chem. C* 113 (2009) 20127–20134, <https://doi.org/10.1021/jp908090s>.
- J. Liu, Z. Wang, J. Zhu, Binder-free nitrogen-doped carbon paper electrodes derived from polypyrrole/cellulose composite for Li-O₂ batteries, *J. Power Sources* 306 (2016) 559–566, <https://doi.org/10.1016/j.jpowsour.2015.12.074>.
- S. Levchenko, V. Marangon, S. Bellani, L. Pasquale, F. Bonaccorso, V. Pellegrini, J. Hassoun, Influence of ion diffusion on the Lithium-oxygen electrochemical process and battery application using carbon nanotubes-graphene substrate, *ACS Appl. Mater. Interfaces* 15 (2023) 39218–39233, <https://doi.org/10.1021/acsaami.3c05240>.
- S. Levchenko, G. Valente, J. Hassoun, A Lithium-oxygen battery exploiting carbon nanotubes, Graphene and Gold Catalyst, *Adv Sustain Syst* 8 (2024) 2400381, <https://doi.org/10.1002/advsu.202400381>.
- L. Carbone, P.T. Moro, M. Gobet, S. Munoz, M. Devany, S.G. Greenbaum, J. Hassoun, Enhanced Lithium oxygen battery using a Glyme electrolyte and carbon nanotubes, *ACS Appl. Mater. Interfaces* 10 (2018) 16367–16375, <https://doi.org/10.1021/acsaami.7b19544>.
- B. Kumar, J. Kumar, R. Leese, J.P. Fellner, S.J. Rodrigues, K.M. Abraham, A. Solid-State, Rechargeable, Long Cycle Life Lithium-Air Battery, *J. Electrochem. Soc.* 157 (2010) A50–A54, <https://doi.org/10.1149/1.3256129>.
- L. Cecchetto, M. Salomon, B. Scrosati, F. Croce, Study of a Li-air battery having an electrolyte solution formed by a mixture of an ether-based aprotic solvent and an ionic liquid, *J. Power Sources* 213 (2012) 233–238, <https://doi.org/10.1016/j.jpowsour.2012.04.038>.
- H.-G. Jung, J. Hassoun, J.-B. Park, Y.-K. Sun, B. Scrosati, An improved high-performance lithium-air battery, *Nat. Chem.* 4 (2012) 579–585, <https://doi.org/10.1038/nchem.1376>.
- J. Hassoun, F. Croce, M. Armand, B. Scrosati, Investigation of the O₂ electrochemistry in a polymer electrolyte solid-state cell, *Angew. Chem. Int. Ed.* 50 (2011) 2999–3002, <https://doi.org/10.1002/anie.2011006264>.
- C.O. Laoire, S. Mukerjee, K.M. Abraham, E.J. Plichta, M.A. Hendrickson, Influence of nonaqueous solvents on the electrochemistry of oxygen in the rechargeable Lithium-air battery, *J. Phys. Chem. C* 114 (2010) 9178–9186, <https://doi.org/10.1021/jp102019y>.
- P.G. Bruce, S.A. Freunberger, L.J. Hardwick, J.-M. Tarascon, Li-O₂ and Li-S batteries with high energy storage, *Nat. Mater.* 11 (2012) 19–29, <https://doi.org/10.1038/nmat3191>.
- J. Ming, Z. Cao, Y. Wu, W. Wahyudi, W. Wang, X. Guo, L. Cavallo, J.-Y. Hwang, A. Shamim, L.-J. Li, Y.-K. Sun, H.N. Alshareef, New insight on the role of electrolyte additives in rechargeable Lithium ion batteries, *ACS Energy Lett.* 4 (2019) 2613–2622, <https://doi.org/10.1021/acseenergylett.9b01441>.
- S. Xiong, K. Xie, Y. Diao, X. Hong, Properties of surface film on lithium anode with LiNO₃ as lithium salt in electrolyte solution for lithium-sulfur batteries, *Electrochim. Acta* 83 (2012) 78–86, <https://doi.org/10.1016/j.electacta.2012.07.118>.
- S.H. Lee, J. Hwang, J. Ming, Z. Cao, H.A. Nguyen, H. Jung, J. Kim, Y. Sun, Toward the sustainable Lithium Metal batteries with a new electrolyte solvation chemistry, *Adv. Energy Mater.* 10 (2020) 2000567, <https://doi.org/10.1002/aenm.202000567>.
- B. Wang, T. Xu, S. Huang, D. Kong, X. Li, Y. Wang, Recent advances in carbon-shell-based nanostructures for advanced Li/Na metal batteries, *J Mater Chem A Mater* 9 (2021) 6070–6088, <https://doi.org/10.1039/D0TA10884G>.
- D. Cao, Q. Zhang, A.M. Hafez, Y. Jiao, Y. Ma, H. Li, Z. Cheng, C. Niu, H. Zhu, Lignin-derived holey, layered, and thermally conductive 3D scaffold for Lithium dendrite suppression, *Small Methods* 3 (2019) 1800539, <https://doi.org/10.1002/SMTD.201800539>.
- Z. Huang, C. Zhang, W. Lv, G. Zhou, Y. Zhang, Y. Deng, H. Wu, F. Kang, Q.-H. Yang, Realizing stable lithium deposition by *in situ* grown Cu₂S nanowires inside commercial Cu foam for lithium metal anodes, *J Mater Chem A Mater* 7 (2019) 727–732, <https://doi.org/10.1039/C8TA10341K>.
- W. Chen, R.V. Salvatierra, M. Ren, J. Chen, M.G. Stanford, J.M. Tour, Laser-induced silicon oxide for anode-free Lithium Metal batteries, *Adv. Mater.* 32 (2020) 2002850, <https://doi.org/10.1002/ADMA.202002850>.
- G. Li, H. Li, Y. Wang, D. Xiong, S. Wang, Y. Yan, S. Chen, B. Tian, Y. Shi, Suppressing Li dendrite puncture with a hierarchical h-BN protective layer, *ACS Appl. Mater. Interfaces* 13 (2021) 56109–56115, <https://doi.org/10.1021/acsaami.1c15980>.
- J. Hassoun, H.-G. Jung, D.-J. Lee, J.-B. Park, K. Amine, Y.-K. Sun, B. Scrosati, A. Metal-Free, Lithium-ion oxygen battery: a step forward to safety in Lithium-air batteries, *Nano Lett.* 12 (2012) 5775–5779, <https://doi.org/10.1021/nl303087j>.
- V. Marangon, C. Hernandez-Rentero, S. Levchenko, G. Bianchini, D. Spagnolo, A. Caballero, J. Morales, J. Hassoun, Lithium-oxygen battery exploiting highly concentrated Glyme-based electrolytes, *ACS Appl. Energy Mater.* 3 (2020) 12263–12275, <https://doi.org/10.1021/acsaem.0c02331>.
- J.-B. Park, J. Hassoun, H.-G. Jung, H.-S. Kim, C.S. Yoon, I.-H. Oh, B. Scrosati, Y.-K. Sun, Influence of temperature on lithium-oxygen battery behavior, *Nano Lett.* 13 (2013) 2971–2975, <https://doi.org/10.1021/nl401439b>.
- D. Di Lecce, V. Marangon, H.-G. Jung, Y. Tominaga, S. Greenbaum, J. Hassoun, Glyme-based electrolytes: suitable solutions for next-generation lithium batteries, *Green Chem.* 24 (2022) 1021–1048, <https://doi.org/10.1039/d1gc39966b>.
- S. Levchenko, S. Wei, V. Marangon, J. Hassoun, A Li-ion battery using nanostructured Sn@C alloying anode and high-voltage LiNi_{0.35}Cu_{0.1}Mn_{1.45}A_{0.1}O₄ spinel cathode, *Energ. Technol.* 10 (2022) 2200725, <https://doi.org/10.1002/ente.202200725>.
- A.E. Del Rio Castillo, V. Pellegrini, A. Ansaldo, F. Ricciardella, H. Sun, L. Marasco, J. Buha, Z. Dang, L. Gagliani, E. Lago, M. Polini, F. Bonaccorso, High-yield

- production of 2D crystals by wet-jet milling, *Mater. Horiz.* 5 (2018) 890–904, <https://doi.org/10.1039/c8mh00487k>.
- [37] K.J. Laidler, The development of the Arrhenius equation, *J. Chem. Educ.* 61 (1984) 494, <https://doi.org/10.1021/ed061p494>.
- [38] J. Evans, C.A. Vincent, P.G. Bruce, Electrochemical measurement of transference numbers in polymer electrolytes, *Polymer (Guildf)* 28 (1987) 2324–2328, [https://doi.org/10.1016/0032-3861\(87\)90394-6](https://doi.org/10.1016/0032-3861(87)90394-6).
- [39] B.A. Boukamp, A nonlinear least squares fit procedure for analysis of immittance data of electrochemical systems, *Solid State Ionics* 20 (1986) 31–44, [https://doi.org/10.1016/0167-2738\(86\)90031-7](https://doi.org/10.1016/0167-2738(86)90031-7).
- [40] B.A. Boukamp, A package for impedance/admittance data analysis, *Solid State Ionics* 18–19 (1986) 136–140, [https://doi.org/10.1016/0167-2738\(86\)90100-1](https://doi.org/10.1016/0167-2738(86)90100-1).
- [41] W.A. Henderson, Glyme-lithium salt phase behavior, *J. Phys. Chem. B* 110 (2006) 13177–13183, <https://doi.org/10.1021/jp061516t>.
- [42] W.A. Henderson, F. McKenna, M.A. Khan, N.R. Brooks, V.G. Young Jr., R. Frech, Glyme-lithium bis(trifluoromethanesulfonyl)imide and glyme-lithium bis(perfluoroethanesulfonyl)imide phase behavior and solvate structures, *Chem. Mater.* 17 (2005) 2284–2289, <https://doi.org/10.1021/cm047881j>.
- [43] V. Marangon, L. Minnetti, E. Barcaro, J. Hassoun, Room-temperature Solid-State polymer electrolyte in Li-LiFePO₄, Li-S and Li-O₂ batteries, *Chem. Eur. J.* 29 (2023) e202301345, <https://doi.org/10.1002/chem.202301345>.
- [44] W. Ghder Soliman, Ch. Swathi, T. Yasasvi, B. Keerthi Priya, D. Akhila Reddy, Review on poly(ethylene oxide)-based electrolyte and anode nanomaterials for the internet of things node-level lithium-ion batteries, *Mater. Today Proc.* 42 (2021) 429–435, <https://doi.org/10.1016/j.matpr.2020.09.806>.
- [45] A. Bartolotta, G. Carini, G. D'Angelo, M. Federico, V. Romano, G. Di Marco, Plasticization, Antiplasticization, and fragility in blends of polyvinyl Butyral and polyethylene glycol dimethyl ether, *Macromol. Chem. Phys.* 224 (2023) 2300158, <https://doi.org/10.1002/macp.202300158>.
- [46] C.A. Gracia-Fernández, S. Gómez-Barreiro, J. López-Beceiro, S. Naya, R. Artiaga, New approach to the double melting peak of poly(L-lactic acid) observed by DSC, *J. Mater. Res.* 27 (2012) 1379–1382, <https://doi.org/10.1557/jmr.2012.57>.
- [47] L. Balo, H. Gupta, S.K. Singh, V.K. Singh, A.K. Tripathi, N. Srivastava, R.K. Tiwari, R. Mishra, D. Meghnani, R.K. Singh, Development of gel polymer electrolyte based on LiTFSI and EMIMFSI for application in rechargeable lithium metal battery with GO-LFP and NCA cathodes, *J. Solid State Electrochem.* 23 (2019) 2507–2518, <https://doi.org/10.1007/s10008-019-04321-6>.
- [48] K.P. Barteau, M. Wolffs, N.A. Lynd, G.H. Fredrickson, E.J. Kramer, C.J. Hawker, Allyl Glycidyl ether-based polymer electrolytes for room temperature Lithium batteries, *Macromolecules* 46 (2013) 8988–8994, <https://doi.org/10.1021/ma401267w>.
- [49] D.H.C. Wong, A. Vitale, D. Devaux, A. Taylor, A.A. Pandya, D.T. Hallinan, J. L. Thelen, S.J. Mecham, S.F. Lux, A.M. Lapides, N.P. Balsara, J.M. Desimone, Phase behavior and electrochemical characterization of blends of perfluoropolyether, poly(ethylene glycol), and a lithium salt, *Chem. Mater.* 27 (2015) 597–603, <https://doi.org/10.1021/cm504228a>.
- [50] I. Rey, J.C. Lassègues, J. Gronclin, L. Servant, Infrared and Raman study of the PEO-LiTFSI polymer electrolyte, *Electrochim. Acta* 43 (1998) 1505–1510, [https://doi.org/10.1016/S0013-4686\(97\)10092-5](https://doi.org/10.1016/S0013-4686(97)10092-5).
- [51] V.S. Patil, K. Vithya, M. Premalatha, B. Sundaresan, FTIR studies on PMMA-LiNO₃ polymer electrolyte, *Macromol. Symp.* 387 (2019) 1800177, <https://doi.org/10.1002/masy.201800177>.
- [52] D. Brouillette, D.E. Irish, N.J. Taylor, G. Perron, M. Odziemkowski, J.E. Desnoyers, Stable solvates in solution of lithium bis(trifluoromethylsulfone)imide in glymes and other aprotic solvents: phase diagrams, crystallography and Raman spectroscopy, *Phys. Chem. Chem. Phys.* 4 (2002) 6063–6071, <https://doi.org/10.1039/b203776a>.
- [53] R.E. Miller, R.R. Getty, K.L. Treuil, G.E. Leroi, Raman Spectrum of crystalline Lithium nitrate, *J. Chem. Phys.* 51 (1969) 1385–1389, <https://doi.org/10.1063/1.1672185>.
- [54] G.M. Veith, J. Nanda, L.H. Delmau, N.J. Dudney, Influence of Lithium salts on the discharge chemistry of Li–air cells, *J. Phys. Chem. Lett.* 3 (2012) 1242–1247, <https://doi.org/10.1021/jz300430s>.
- [55] Ó. Vargas, Á. Caballero, J. Morales, E. Rodríguez-Castellón, Contribution to the understanding of capacity fading in graphene Nanosheets acting as an anode in full Li-ion batteries, *ACS Appl. Mater. Interfaces* 6 (2014) 3290–3298, <https://doi.org/10.1021/am405197s>.
- [56] D. Di Lecce, V. Marangon, A. Benítez, Á. Caballero, J. Morales, E. Rodríguez-Castellón, J. Hassoun, High capacity semi-liquid lithium sulfur cells with enhanced reversibility for application in new-generation energy storage systems, *J. Power Sources* 412 (2019) 575–585, <https://doi.org/10.1016/j.jpowsour.2018.11.068>.
- [57] A. Schechter, D. Aurbach, H. Cohen, X-ray photoelectron spectroscopy study of surface films formed on Li electrodes freshly prepared in alkyl carbonate solutions, *Langmuir* 15 (1999) 3334–3342, <https://doi.org/10.1021/la981048h>.
- [58] D. Enslin, M. Stjernedahl, A. Nytén, T. Gustafsson, J.O. Thomas, A comparative XPS surface study of Li₂ FeSiO₄/C cycled with LiTFSI- and LiPF₆-based electrolytes, *J. Mater. Chem.* 19 (2009) 82–88, <https://doi.org/10.1039/B813099J>.
- [59] Q. Liu, A. Cresce, M. Schroeder, K. Xu, D. Mu, B. Wu, L. Shi, F. Wu, Insight on lithium metal anode interphasial chemistry: reduction mechanism of cyclic ether solvent and SEI film formation, *Energy Storage Mater.* 17 (2019) 366–373, <https://doi.org/10.1016/j.ensm.2018.09.024>.
- [60] M. Tulodziecki, J.-M. Tarascon, P.-L. Taberna, C. Guéry, Catalytic reduction of TFSI-containing ionic liquid in the presence of lithium cations, *Electrochem. Commun.* 77 (2017) 128–132, <https://doi.org/10.1016/j.elecom.2017.02.014>.
- [61] R. Demir-Cakan, M. Morcrette, A. Gangulibabu, R. Guéguen, J.-M. Dedryvère, Tarascon, Li-S batteries: simple approaches for superior performance, *Energy, Environ. Sci.* 6 (2013) 176–182, <https://doi.org/10.1039/c2ee23411d>.
- [62] M. Agostini, S. Xiong, A. Matic, J. Hassoun, Polysulfide-containing Glyme-based electrolytes for Lithium sulfur battery, *Chem. Mater.* 27 (2015) 4604–4611, <https://doi.org/10.1021/acs.chemmater.5b00896>.
- [63] K.P.C. Yao, D.G. Kwabi, R.A. Quinlan, A.N. Mansour, A. Grimaud, Y.-L. Lee, Y.-C. Lu, Y. Shao-Horn, Thermal stability of Li₂O₂ and Li₂O for Li-air batteries: In Situ XRD and XPS Studies, *J. Electrochem. Soc.* 160 (2013) A824–A831, <https://doi.org/10.1149/2.069306jes>.
- [64] S. Wei, S. Inoue, D. Di Lecce, Z. Li, Y. Tominaga, J. Hassoun, Towards a high-performance Lithium-Metal battery with Glyme solution and an olivine cathode, *ChemElectroChem* 7 (2020) 2376–2388, <https://doi.org/10.1002/CELC.202000272>.
- [65] A.M. Andersson, A. Henningson, H. Siegbahn, U. Jansson, K. Edström, Electrochemically lithiated graphite characterised by photoelectron spectroscopy, *J. Power Sources* 119–121 (2003) 522–527, [https://doi.org/10.1016/S0378-7753\(03\)00277-5](https://doi.org/10.1016/S0378-7753(03)00277-5).
- [66] D. Aurbach, M.D. Levi, E. Levi, A. Schechter, Failure and stabilization mechanisms of graphite electrodes, *J. Phys. Chem. B* 101 (1997) 2195–2206, <https://doi.org/10.1021/jp962815t>.
- [67] C. Hernández-Enterero, V. Marangon, M. Olivares-Marín, V. Gómez-Serrano, Á. Caballero, J. Morales, J. Hassoun, Alternative lithium-ion battery using biomass-derived carbons as environmentally sustainable anode, *J. Colloid Interface Sci.* 573 (2020) 396–408, <https://doi.org/10.1016/j.jcis.2020.03.092>.
- [68] I. Ismail, A. Noda, A. Nishimoto, M. Watanabe, XPS study of lithium surface after contact with lithium-salt doped polymer electrolytes, *Electrochim. Acta* 46 (2001) 1595–1603, [https://doi.org/10.1016/S0013-4686\(00\)00758-1](https://doi.org/10.1016/S0013-4686(00)00758-1).
- [69] Y.S. Cohen, Y. Cohen, D. Aurbach, Micromorphological studies of Lithium electrodes in alkyl carbonate solutions using in situ atomic force microscopy, *J. Phys. Chem. B* 104 (2000) 12282–12291, <https://doi.org/10.1021/jp002526b>.
- [70] S.S. Zhang, Role of LiNO₃ in rechargeable lithium/sulfur battery, *Electrochim. Acta* 70 (2012) 344–348, <https://doi.org/10.1016/j.electacta.2012.03.081>.
- [71] G.A. Elia, J.-B. Park, Y.-K. Sun, B. Scrosati, J. Hassoun, Role of the lithium salt in the performance of lithium-oxygen batteries: a comparative study, *ChemElectroChem* 1 (2014) 47–50, <https://doi.org/10.1002/celec.201300160>.
- [72] G.A. Elia, D. Bresser, J. Reiter, P. Oberhumer, Y.-K. Sun, B. Scrosati, S. Passerini, J. Hassoun, Interphase evolution of a Lithium-ion/oxygen battery, *ACS Appl. Mater. Interfaces* 7 (2015) 22638–22643, <https://doi.org/10.1021/acsami.5b07414>.
- [73] J. Hassoun, P. Ochal, S. Panero, G. Mulas, C. Bonatto Minella, B. Scrosati, The effect of CoSn/CoSn₂ phase ratio on the electrochemical behaviour of Sn₄₀Co₄₀C₂₀ ternary alloy electrodes in lithium cells, *J. Power Sources* 180 (2008) 568–575, <https://doi.org/10.1016/j.jpowsour.2008.01.059>.
- [74] H. Deng, F. Qiu, X. Li, H. Qin, S. Zhao, P. He, H. Zhou, A Li-ion oxygen battery with Li-Si alloy anode prepared by a mechanical method, *Electrochem. Commun.* 78 (2017) 11–15, <https://doi.org/10.1016/j.elecom.2017.03.010>.
- [75] T. Zhang, K. Liao, P. He, H. Zhou, A self-defense redox mediator for efficient lithium-O₂ batteries, *Energy Environ. Sci.* 9 (2015) 1024–1030, <https://doi.org/10.1039/C5EE02803E>.